Single droplet or bubble and its stability: Kinetic theory and dynamical system approaches

Takumu Miyauchi [*] and Shigeru Takata [†]
Department of Aeronautics and Astronautics, Kyoto University, Kyoto-daigaku-katsura, Kyoto 615-8540, Japan

(Received 1 May 2024; accepted 1 August 2024; published 21 August 2024)

Steady solutions of a single droplet or bubble in the van der Waals fluid are investigated on the basis of the kinetic model equation that has been recently proposed by Miyauchi *et al.* [*Gas Dynamics with Applications in Industry and Life Sciences* (Springer, Cham, 2023), pp. 19–39]. Under the thermal equilibrium condition and isotropic assumption with respect to the origin of the coordinates, the kinetic equation is reduced to an ordinary differential equation for the density, which can be regarded as a low-dimensional dynamical system. The possible density distribution is studied as a *flow* in the low-dimensional phase space. It is clarified that a single droplet or bubble can be understood as a *flow* that goes into a fixed point and that the *flow* is qualitatively different in the unstable and metastable parameter regions. The features of the obtained density distributions in individual regions are also clarified. Finally, the stability of those solutions is studied by direct numerical experiments of the kinetic equation.

DOI: 10.1103/PhysRevE.110.025102

I. INTRODUCTION

Two-phase systems with or without the phase change have been variously studied so far by the thermal-fluid-dynamic way from the physics, chemical physics, mathematical physics, and engineering point of view. When the dynamic aspects are of interest, the Cahn–Hilliard equation [1] or its variants have been widely used in the thermodynamic discussions, while the Navier–Stokes equation for two-phase fluids has been used in the fluid dynamic discussions (e.g., Refs. [2,3]). However, the dynamic process does not necessarily occur under the phase equilibrium. This is the point that has motivated studies using microscopic approaches that are free from the phase equilibrium constraint in recent decades. Molecular dynamics (MD) [4–6] and kinetic theory [7–12] are typical approaches taken in such studies.

Probably the most fundamental setting for understanding the elementary process of the phase change from a single to a two-phase state would be the problem of a single droplet or bubble in the infinite expanse of the fluid. Such a setting is the simplest, at least conceptually, but is not necessarily well understood. For instance, though some MD simulations can be found in the literature, they are usually conducted under a periodic condition. Therefore, in drawing conclusions about single droplet (or bubble) formation from those simulations, we need to examine carefully whether there are still interactions with other droplets or bubbles, whether the simulation is for an energy conservative or isothermal system, and so on. Our previous 1D simulations using a kinetic model equation [8,11] are not exception as well, and they do not provide direct information about the single droplet (or bubble) formation.

With this background, Busuioc *et al.* [12] recently conducted numerical simulations of a single bubble on the basis of the Enskog–Vlasov equation [13]. However, their main goal is to develop a stochastic particle simulation method for the Enskog–Vlasov equation. In the present paper, we more focus on the analysis of a steady single droplet or bubble and its stability, thereby deepening our understanding of the elementary process in phase change. The dynamics-like interpretation of the phase change in the context of van der Waals fluids can be traced back to, for example, the work by van Kampen [14,15] based on the equilibrium statistical thermodynamics. He clearly explained the two-phase equilibrium in terms of the thermodynamical potential by the resemblance with a classical point mass dynamics, especially for one-dimensional case. Indeed, we have made use of his interpretation in our previous work [16] for the discussion of one-dimensional case. In the present work, we shall step forward to multidimensional cases that require more detailed study of the dynamical system, thereby showing peculiar features that is absent from one-dimensional case.

The main ingredients of the present study are the low-dimensional dynamical system analysis [17,18] on the steady solution and simple numerical simulations for the instability assessment of the steady solution via the kinetic model developed in Ref. [19]. Our approach is thus distinctive to the order-parameter models with fluctuations [20] in the literature. In the simulations in Sec. V, physical (thermal) fluctuations are not added to the single droplet (or bubble) solution obtained in the study of dynamical system to be discussed in Sec. IV D. Instead, the numerical errors coming from discretization and numerical approximations play the role of fluctuations there. Hence, the collapse of the single droplet or bubble to be observed in Sec. IV D simply suggests that such a droplet or bubble is linearly unstable.

The paper is organized as follows. First, the kinetic model that our analysis is based on is presented in Sec. II. The

[*]Contact author: miyauchi.takumu.23e@st.kyoto-u.ac.jp
[†]Contact author: takata.shigeru.4a@kyoto-u.ac.jp

model was proposed in Ref. [19] as an extension of our previous models [11,16]. The H-theorem and the reproducibility of appropriate transport properties were established for the model. Next in Sec. III, steady solutions of a single droplet or bubble that is isotropic to the origin of the coordinates are investigated within the uniform resting Maxwellians and the problem is reduced to the one for the radial density field. The reduced problem is treated and studied as a low-dimensional dynamical system in Sec. IV by using the concepts of the phase space vector field, fixed point, and *flow* [21] that are familiar in the field of nonlinear dynamical system [17,18]. In particular, it will be clarified in Sec. IV C that the *flow* changes qualitatively whether the pair of parameters of the far-field uniform state falls into the unstable region or the metastable region [11,22]. The structure of the single droplet or bubble will be also discussed in Sec. IV D. In Sec. V, the instability of the obtained steady solution is assessed by direct numerical simulations of the kinetic model. The paper is concluded in Sec. VI.

II. KINETIC MODEL EQUATION

We study a single droplet or bubble in an infinite expanse of the van der Waals fluid using the kinetic model proposed in Ref. [19] under the name of the second ellipsoidal-statistical (ES)-based model:

$$\frac{\partial f}{\partial t}+\xi_i\frac{\partial f}{\partial X_i}+F_i\frac{\partial f}{\partial \xi_i}=Q_c^\flat[f]+Q_d^\flat[f], \tag{1a}$$

$$f\to\frac{\rho_\infty}{(2\pi RT_\infty)^{\frac{3}{2}}}\exp\left(-\frac{\xi_i^2}{2RT_\infty}\right),\quad (|\boldsymbol{X}|\to\infty), \tag{1b}$$

where t is time, $\boldsymbol{X}$ (or X_i) is spatial position, $\boldsymbol{\xi}$ (or ξ_i) is molecular velocity, $f(t,\boldsymbol{X},\boldsymbol{\xi})$ is the velocity distribution function (VDF), R is the specific gas constant, and ρ_∞ and T_∞ are positive constants for the far-field density and temperature, respectively. $Q_c^\flat$ is the ES-type collision model [23,24] given by

$$Q_c^\flat[f]=A^\flat(\rho,T)(\mathcal{G}-f), \tag{2}$$

$$\mathcal{G}=\frac{\rho}{\sqrt{\det(2\pi\mathcal{T})}}\exp\left(-\frac{1}{2}(\mathcal{T}^{-1})_{ij}c_ic_j\right), \tag{3}$$

$$c_i=\xi_i-v_i,\quad \mathcal{T}_{ij}=(1-\nu)RT\delta_{ij}+\nu\Theta_{ij}, \tag{4}$$

$$\rho=\int f d\boldsymbol{\xi},\quad v_i=\frac{1}{\rho}\int \xi_i f d\boldsymbol{\xi}, \tag{5}$$

$$T=\frac{1}{3\rho R}\int c_k^2 f d\boldsymbol{\xi},\quad \Theta_{ij}=\frac{1}{\rho}\int c_ic_j f d\boldsymbol{\xi}. \tag{6}$$

Here, ν is an adjusting parameter for the Prandtl number in the range $-1/2\leqslant\nu<1$. $\mathcal{T}^{-1}$ is the inverse of the tensor $\mathcal{T}$. ρ, $\boldsymbol{v}$ (or v_i), and T are, respectively, the density, flow velocity, and temperature. $Q_d^\flat$ is a correction term to $Q_c^\flat$ for exclusive effects of molecules and $\boldsymbol{F}$ (or F_i) is a force acting on a molecule per unit mass. They are assumed to take the form:

$$Q_d^\flat[f]=-\frac{\partial}{\partial\xi_i}\left[(\alpha_i^\flat+\beta^\flat c_i)f\right], \tag{7}$$

$$F_i=-\frac{\partial}{\partial X_i}(\Phi_S+\Phi_L). \tag{8}$$

There are still some quantities that should be specified. In the above, F_i is composed of two potential forces: the long-range Φ_L and short-range Φ_S. Φ_L is purely attractive and can be expressed within the diffusion approximation [11,16] as

$$\Phi_L=-\kappa\frac{\partial^2\rho}{\partial X_i^2}, \tag{9}$$

where κ is a positive constant. Φ_S is a combined potential of repulsion and attraction and, by applying a local approximation due to the short-range nature, its form can be specified, together with $A^\flat$, in accordance with the equation of state for the van der Waals fluid [11,16]:

$$p=\frac{\rho RT}{1-b\rho}-a\rho^2,\quad (0<b\rho<1), \tag{10}$$

as follows:

$$\Phi_S=-RT\ln(1-b\rho)+\frac{b\rho RT}{1-b\rho}-2a\rho, \tag{11}$$

$$A^\flat=\frac{5}{2}\frac{\rho RT}{1-b\rho}\frac{R}{\lambda_0(T)}. \tag{12}$$

Here p is the pressure, a and b are positive constant, and λ_0 is the thermal conductivity in the dilute gas limit. Moreover, by setting the viscosity and thermal conductivity to those of the Enskog equation [25,26], all the remaining quantities can be specified as

$$\alpha_i^\flat=\alpha_i+\frac{1}{\rho}\left[\mu_P\overline{\frac{\partial v_i}{\partial X_j}}+\mu_B\frac{\partial v_k}{\partial X_k}\delta_{ij}\right], \tag{13}$$

$$\beta^\flat=\beta+\frac{1}{3\rho RT}\left\{\frac{\partial}{\partial X_k}\left(\lambda_P\frac{\partial T}{\partial X_k}\right)+\frac{\partial v_i}{\partial X_j}\left[\mu_P\overline{\frac{\partial v_i}{\partial X_j}}+\mu_B\frac{\partial v_k}{\partial X_k}\delta_{ij}\right]\right\}, \tag{14}$$

$$\alpha_i=\frac{1}{\rho}\int\frac{\partial\Phi_S}{\partial T}d\rho\frac{\partial T}{\partial X_i}, \tag{15}$$

$$\beta=\frac{1}{3\rho R}\left\{\frac{\partial}{\partial t}\int\frac{\partial\Phi_S}{\partial T}d\rho+\frac{\partial}{\partial X_i}\left(v_i\int\frac{\partial\Phi_S}{\partial T}d\rho\right)\right\}, \tag{16}$$

$$\overline{\frac{\partial v_i}{\partial X_j}}=\frac{\partial v_i}{\partial X_j}+\frac{\partial v_j}{\partial X_i}-\frac{2}{3}\frac{\partial v_k}{\partial X_k}\delta_{ij}, \tag{17}$$

$$\mu_P=(1-b\rho)g_1^\flat\left(\frac{b\rho}{1-b\rho}\right)\mu_0(T), \tag{18}$$

$$\mu_B=(1-b\rho)\left(\frac{b\rho}{1-b\rho}\right)^2\mu_0(T), \tag{19}$$

$$\lambda_P=(1-b\rho)g_2^\flat\left(\frac{b\rho}{1-b\rho}\right)\lambda_0(T), \tag{20}$$

$$\mathrm{Pr}_0=\frac{5}{2}R\frac{\mu_0}{\lambda_0}=\frac{2}{3},\quad \nu=1-\frac{1}{\mathrm{Pr}_0}=-\frac{1}{2}, \tag{21}$$

$$g_1^\flat(x)=\frac{4}{5}x+\frac{6.1}{8}x^2,\quad g_2^\flat(x)=\frac{6}{5}x+\frac{12.1}{16}x^2. \tag{22}$$

Here, additional comments would be in order. μ_P, μ_B, and λ_P represent the exclusion effect of molecules on the viscosity, bulk viscosity, and thermal conductivity, respectively. μ_0 and Pr_0 represent the viscosity and the Prandtl number in the

dilute gas limit. For the above kinetic model equation with the quantities so specified, the H-theorem has been shown to hold for periodic systems in Ref. [19]. This completes the presentation of the kinetic model used in the remainder of the paper.

III. STEADY SINGLE DROPLET OR BUBBLE ISOTROPIC TO THE ORIGIN

In the present section, a steady single droplet (or bubble) in an infinite expanse of the van der Waals fluid will be considered. Since such a single droplet (or bubble) is in the thermal equilibrium state, the solution is sought within the resting Maxwellian with uniform temperature T_∞ (see Appendix A):

$$f(\boldsymbol{X},\boldsymbol{\xi}) = \frac{\rho(\boldsymbol{X})}{(2\pi RT_\infty)^{3/2}} \exp\left(-\frac{\boldsymbol{\xi}^2}{2RT_\infty}\right). \tag{23}$$

By substitution of Eq. (23), Eq. (1a) is reduced to

$$\frac{\partial}{\partial X_i}(RT_\infty \ln\rho + \Phi_S + \Phi_L) = 0. \tag{24}$$

Integrating Eq. (24) once with respect to $\boldsymbol{X}$ and substituting Eqs. (9) and (11) reduces the original problem, Eq. (1), to a much simpler form:

$$\kappa\frac{\partial^2\rho}{\partial X_i^2} = RT_\infty\left(\ln\frac{b\rho}{1-b\rho} + \frac{1}{1-b\rho} - \lambda_*\right) - 2a\rho, \tag{25a}$$

$$\rho \to \rho_\infty, \quad (|\boldsymbol{X}| \to \infty). \tag{25b}$$

Here λ_* is a dimensionless constant that is related to ρ_∞ and T_∞. Indeed, since $\rho \to \rho_\infty$ as $\boldsymbol{X} \to \infty$ by Eq. (25b), $\partial^2\rho/\partial X_i^2 \to 0$ in the same limit, leading to the relation

$$RT_\infty\left(\ln\frac{b\rho_\infty}{1-b\rho_\infty} + \frac{1}{1-b\rho_\infty} - \lambda_*\right) = 2a\rho_\infty. \tag{26}$$

In the meantime, the critical density ρ_c and temperature T_c are related to the van der Waals constants a and b as

$$3\rho_c = \frac{1}{b}, \quad T_c = \frac{8a}{27Rb}. \tag{27}$$

Hence, the dimensionless quantities

$$\eta = b\rho\left(=\frac{\rho}{3\rho_c}\right), \quad \tilde{T} = \frac{T}{T_c}, \quad x_i = \frac{X_i}{L}, \tag{28}$$

are naturally introduced with $3\rho_c$, T_c, and

$$L = \sqrt{\frac{\kappa}{bRT_c}}, \tag{29}$$

being the reference density, temperature, and length, respectively. Then, Eq. (25) is recast as

$$\frac{\partial^2\eta}{\partial x_i^2} = \Pi(\eta;\eta_\infty,\tilde{T}_\infty), \tag{30a}$$

$$\eta \to \eta_\infty, \quad (|\boldsymbol{x}| \to \infty), \tag{30b}$$

where $\eta_\infty = b\rho_\infty$, $\tilde{T}_\infty = T_\infty/T_c$, and

$$\Pi(\eta;\eta_\infty,\tilde{T}_\infty) \equiv \tilde{T}_\infty[\Lambda(\eta,\tilde{T}_\infty) - \Lambda(\eta_\infty,\tilde{T}_\infty)], \tag{30c}$$

$$\Lambda(X,Y) \equiv \ln\left(\frac{X}{1-X}\right) + \frac{1}{1-X} - \frac{27}{4}\frac{X}{Y}, \tag{30d}$$

$$\lambda_* = \Lambda(\eta_\infty,\tilde{T}_\infty). \tag{30e}$$

Note that Π has two parameters, η_∞ and $\tilde{T}_\infty$, but its variation with respect to η is characterized only by $\tilde{T}_\infty$. Π has two extrema below the critical temperature ($\tilde{T}_\infty < 1$), but above the critical temperature ($\tilde{T}_\infty \geqslant 1$) it increases monotonically with respect to η; see Fig. 1. In fact, Π is a dimensionless version of the specific Gibbs free energy [11], and thus appears later in the thermodynamic discussion of phase equilibrium. In the sequel, η_∞ and $\tilde{T}_\infty$ will be suppressed in the argument of Π, unless confusion is anticipated.

Since our aim is to study a steady single droplet or bubble, it is enough to consider the isotropic field with respect to the origin of the coordinates. Hence, η is assumed to be a function of the radius $r \equiv |\boldsymbol{x}|$ ($\boldsymbol{x} \in \mathbb{R}^D$ with D being the spatial dimension [27]) only and Eq. (30) is further reduced to

$$\frac{1}{r^{D-1}}\frac{d}{dr}\left(r^{D-1}\frac{d\eta}{dr}\right) = \Pi(\eta), \quad (0 \leqslant r < \infty), \tag{31a}$$

$$\eta(r) \to \eta_\infty, \quad (r \to \infty). \tag{31b}$$

We seek nonuniform solutions of Eq. (31) that satisfy $\eta(0) = \eta_O(\neq\eta_\infty)$, $d\eta/dr(0) = 0$ at the origin and $\eta \to \eta_\infty$ as $r \to \infty$. Since these conditions at the origin and at a far field are too many for the second order differential equation, such solutions do not always exist. Hence, putting aside the condition (31b), we shall first consider Eq. (31a) under only the condition at the origin

$$\eta(0) = \eta_O, \quad \frac{d\eta}{dr}(0) = 0, \tag{32}$$

transform it to a system of simultaneous first-order ordinary differential equations, and then study the resulting system as *flows* in low-dimensional phase space [17,18]. Among such *flows*, the steady solution of a single droplet or bubble is chosen as a *flow* that satisfies the far-field condition (31b).

IV. *FLOWS* IN PHASE SPACE

A. Preliminary analysis

In the present subsection, as a preliminary analysis, we consider the behavior of the dimensionless density η qualitatively on the basis of

$$\frac{d\eta}{dr} = \int_0^r \Pi(\eta(s))\left(\frac{s}{r}\right)^{D-1} ds, \tag{33}$$

that is obtained by integrating Eq. (31a) multiplied with r^{D-1} and using the condition (32).

As is clear from Eq. (33), the property of $\Pi(\eta)$ determines whether η increases or decreases with respect to r. As is mentioned in Sec. III and shown in Fig. 1, $\Pi(\eta)$ is monotonic when $\tilde{T}_\infty \geqslant 1$ and has two extrema when $\tilde{T}_\infty < 1$. Thus, $\Pi(\eta)$ has only one zero [Fig. 1(a)] when $\tilde{T}_\infty \geqslant 1$. When $\tilde{T}_\infty < 1$, $\Pi(\eta)$ has at most three zeros and the number of zeros depends

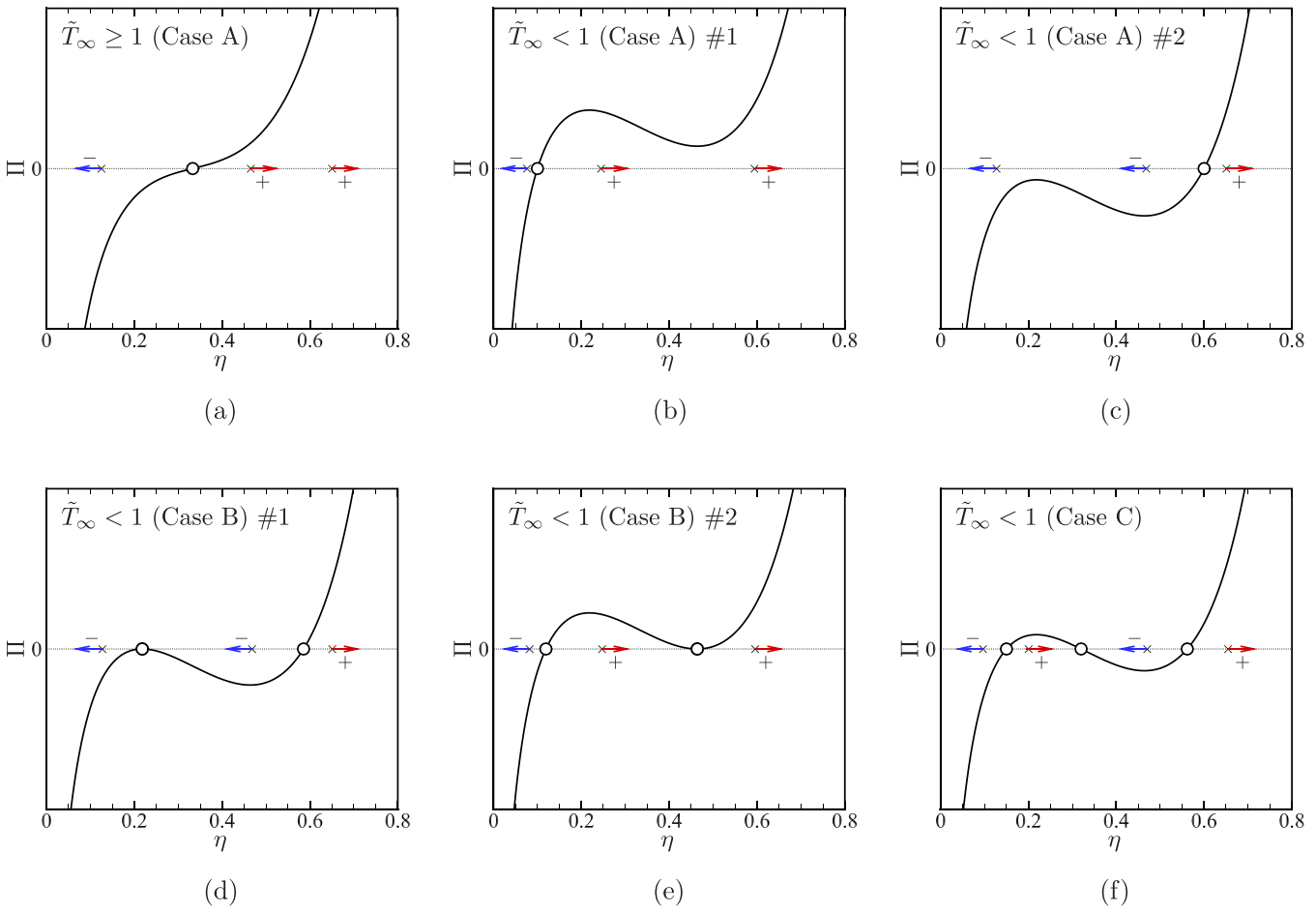

FIG. 1. Classification of $\Pi(\eta)$ and phase-portrait-like diagram. $\Pi(\eta)$ has only one zero point in Case A, two zero points in Case B, and three zero points in Case C, respectively. (a) Case A with $\tilde{T}_\infty \geqslant 1$. (b) Case A with $\tilde{T}_\infty < 1$ and the extrema are positive. (c) Case A with $\tilde{T}_\infty < 1$ and the extrema are negative. (d) Case B and the local maximum is zero. (e) Case B and the local minimum is zero. (f) Case C. In each panel, the arrow indicates the change direction of η starting from η_O at the point $\times$, while $+$ and $-$ indicate the sign of the corresponding value of $\int_0^r \Pi(\eta(s))(s/r)^{D-1}ds$.

on the value of η_∞ [Figs. 1(b)–1(f)]. But in any case $\eta = \eta_\infty$ is always a zero of $\Pi(\eta)$.

First the following proposition holds.

Proposition. If $\Pi(\eta)$ has one or two zeros, then there is no spatially nonuniform solution of Eq. (31).

Proof. First suppose that $\Pi(\eta)$ has only one zero [Case A: Figs. 1(a)–1(c)]. Obviously, this zero is $\eta = \eta_\infty$. Hence, for $\eta_O \lessgtr \eta_\infty$, $\Pi(\eta_O) \lessgtr 0$ holds [Figs. 1(a)–1(c)], and furthermore $d\eta/dr \lessgtr 0$ holds by Eq. (33). This means that the change of η from η_O ($\lessgtr \eta_\infty$) to η_∞ is not possible.

Next suppose that $\Pi(\eta)$ has two zeros. Then, one of the zeros is an extremum point [Case B: Figs. 1(d)–1(e)]. By repeating the same discussion as in the previous case, it is readily seen that both zeros cannot be reached by starting from η_O larger or smaller than both zeros. However, the extremum point might be reached if starting from η_O between two zeros (there is no way to reach the other zero). Therefore, the extremum point is a candidate of η_∞. However, since $\Pi(\eta)$ is either positive definite or negative definite in the process of reaching the extremum point, $d\eta/dr \neq 0$ by Eq. (33) at the extremum point. This means that η cannot approach a certain constant as $r \to \infty$ and the extremum point cannot be η_∞. ■

Thanks to the above Proposition, we can focus on the case that $\Pi(\eta)$ has three zeros [Case C: Fig. 1(f)]. Let η_a, η_b, and η_c be the three zeros ($\eta_a < \eta_b < \eta_c$). Then $\Pi(\eta)$ has one inflection point $\eta = 1/3$, which always lies between the two extrema. Since the inflection point lies between the two extrema and the two extrema lie between η_a and η_c, $\eta_a < 1/3 < \eta_c$ holds. In addition, it is readily seen that $\Pi'(\eta_a) > 0$, $\Pi'(\eta_b) < 0$, and $\Pi'(\eta_c) > 0$ hold as well, where $\Pi' = d\Pi/d\eta$. Again along the same lines as the one zero case in the proof, it is seen that any zeros of $\Pi(\eta)$ cannot be reached starting from η_O larger than η_c or smaller than η_a. To reach zero, $\eta_a < \eta_O < \eta_c$ is required at least. However, in the present stage, the process of approaching zero is not so obvious [28]. The three zeros can be candidates of η_∞. When η_∞ is the middle zero η_b, $\Pi'(\eta_\infty) = \Pi'(\eta_b) < 0$ holds, implying from Eqs. (30c) and (30d) that

$$\tilde{T}_\infty < \frac{27}{4}\eta_\infty(1-\eta_\infty)^2 (\leqslant 1)$$
$$\Leftrightarrow\ a > \frac{RT_\infty}{2\rho_\infty(1-b\rho_\infty)^2}. \tag{34}$$

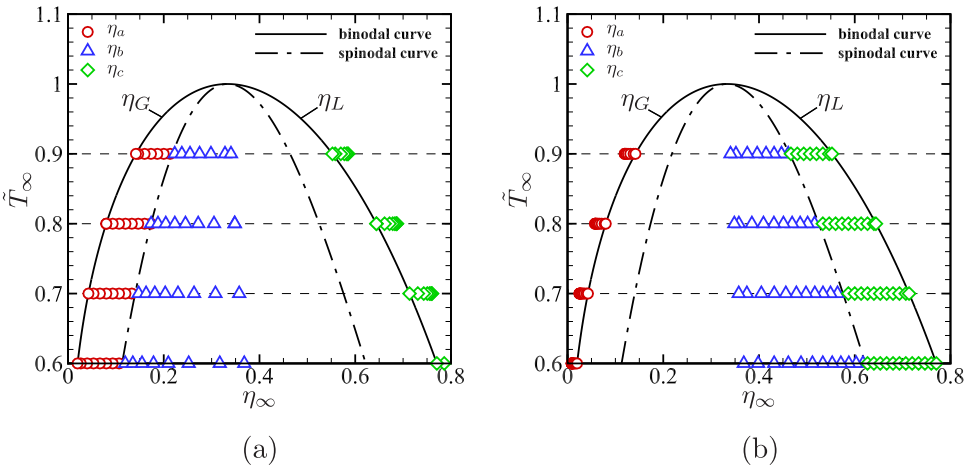

FIG. 2. Parameter diagram in $\eta_\infty \tilde{T}_\infty$ plane. Dashed-dotted: Spinodal curve (35). Solid line: Binodal curve (36). Outside of binodal curve is the stable region, inside of spinodal curve is the unstable region, and between the spinodal and the binodal curve is the metastable region. Open circles (red), triangles (blue), and diamonds (green), respectively, indicate examples of η_a, η_b, and η_c (three zeros of Π) at $\tilde{T}_\infty = 0.6$, 0.7, 0.8, and 0.9. (a) The case where $\eta_\infty = \eta_a$ lies in the metastable region (droplet). (b) The case where $\eta_\infty = \eta_c$ lies in the metastable region (bubble).

This is identical to the parameter region where a uniform resting equilibrium state is unstable and the so-called spinodal decomposition is expected to occur (unstable region) [11]; see Fig. 2. Therefore, if the solution with $\eta_\infty = \eta_b$ is found, it represents a single droplet or bubble in the unstable region. When η_∞ is the minimum or maximum zero (η_a or η_c), $\Pi'(\eta_\infty) > 0$ holds and the inequality in condition (34) is reversed. Hence, if the solution with $\eta_\infty = \eta_a$ or $\eta_\infty = \eta_c$ is found, it represents a single droplet or bubble outside of the unstable region. The pair $(\eta_\infty, \tilde{T}_\infty)$ for such a solution is expected to fall in the metastable region. The metastable region is the one bounded by the spinodal curve

$$\tilde{T}_\infty = \frac{27}{4}\eta_\infty(1-\eta_\infty)^2 (\leqslant 1), \tag{35}$$

and the binodal curve that is obtained by eliminating η_O from the following two equalities [29]:

$$\Pi(\eta_O) = \Pi(\eta_\infty), \quad p(\eta_O, \tilde{T}_\infty) = p(\eta_\infty, \tilde{T}_\infty); \tag{36}$$

see Fig. 2. The binodal line has two branches when regarded as a function of $\tilde{T}_\infty$. For later convenience, let η_L be the branch giving the larger value of η_∞ and let η_G be the branch giving the smaller value, respectively.

B. Set up for *flow* analyses

Let us first introduce the following variables η_1, η_2, η_3 that are functions of r:

$$\eta_1(r) \equiv \eta(r), \quad \eta_2(r) \equiv \frac{d\eta}{dr}, \quad \eta_3(r) \equiv r, \tag{37}$$

and rewrite Eq. (31a) as a set of ordinary differential equations [17]:

$$\frac{d\eta_1}{dr} = \eta_2, \tag{38a}$$

$$\frac{d\eta_2}{dr} = -\frac{D-1}{\eta_3}\eta_2 + \Pi(\eta_1), \tag{38b}$$

$$\frac{d\eta_3}{dr} = 1. \tag{38c}$$

The right-hand side of Eq. (38) gives a three-dimensional constant phase vector field that is characterized by far-field parameters η_∞ and $\tilde{T}_\infty$. The projection of the trajectory in the phase space on the $\eta_1\eta_2$ plane has three fixed points $(\eta_a, 0)$, $(\eta_b, 0)$, and $(\eta_c, 0)$. Since Π does not change whether $\eta_\infty = \eta_a$, η_b, or η_c, the fixed points are common for $\eta_\infty = \eta_a$, η_b, or η_c.

The *flow* with respect to r is determined by Eq. (38) with the condition

$$(\eta_1, \eta_2, \eta_3) = (\eta_O, 0, 0), \quad (r = 0), \tag{39}$$

and the *flow* representing a single droplet or bubble is the one that further satisfies the condition

$$(\eta_1, \eta_2, \eta_3) \to (\eta_\infty, 0, \infty), \quad (r \to \infty). \tag{40}$$

In Sec. IV C, we will study the *flows* numerically, classify them, and identify the conditions under which a steady single droplet (or bubble) solution can be found.

C. Results: Trajectory of *flow* and classification

Equation (38) with Eq. (39) is solved by the fourth-order Runge-Kutta method [30] after a uniform discretization with respect to r. The step size Δr of r is uniform and set as $\Delta r = 1.0 \times 10^{-5}$. The step size was enough fine to draw firm conclusions for the discussions below about the *flow* properties.

1. Case D = 1

Let us start with the spatially one-dimensional case ($D = 1$), since it provides a clear-cut-off of main features of the present dynamical system. Since the first term on the right-hand side of Eq. (38b) vanishes, the vector field does not depend on η_3. Hence, the problem is reduced to the two-dimensional dynamical system on the $\eta_1\eta_2$ plane. The three points $(\eta_\alpha, 0)$ $(\alpha = a, b, c)$ on the η_1 axis are indeed fixed points of the reduced set of Eqs. (38a) and (38b) on the $\eta_1\eta_2$

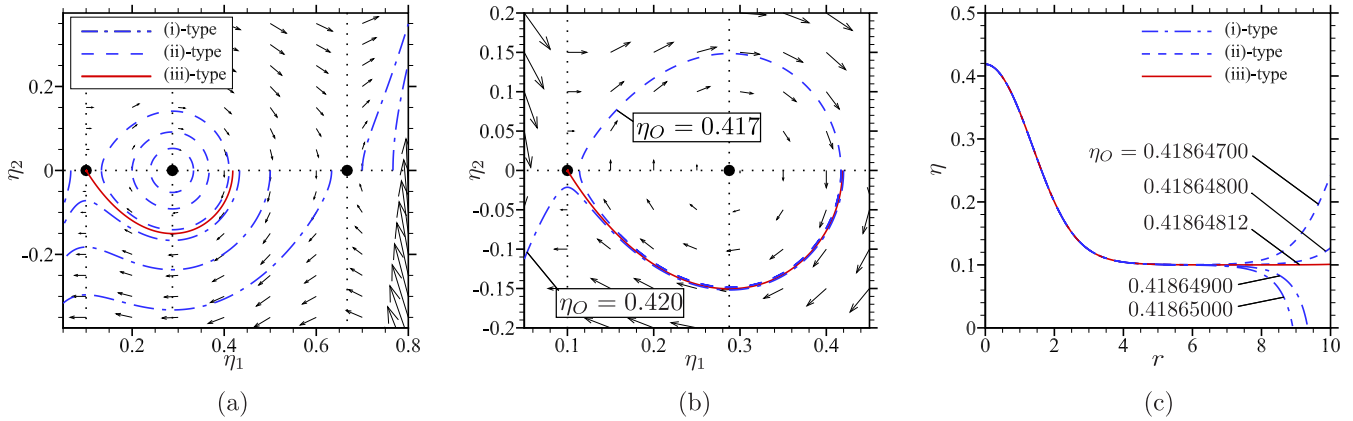

FIG. 3. Vector field, trajectory, and corresponding radial density distribution in the case $D = 1$ for $\eta_\infty = 0.1$ and $\tilde{T}_\infty = 0.8$. (a) Vector field and some trajectory samples. (b) Close-up of critical and near-critical trajectories. (c) Radial density distributions of the trajectories. In panels (a) and (b), closed circles indicate the fixed points in the $\eta_1\eta_2$ plane, the dashed-dotted (blue), the dashed (blue), and the solid (red) line indicate the (i)-type, (ii)-type, and (iii)-type trajectory, respectively.

plane. Since η_∞ is a zero of Π, it must coincide with η_a, η_b, or η_c.

Figure 3(a) shows the vector field in the case $(\eta_\infty, \tilde{T}_\infty) = (0.1, 0.8)$. The pair of the parameters lies in the metastable region and three zeros of Π, i.e., η_a, η_b, and η_c, are 0.1, 0.287521, and 0.667059 in this example; see Fig. 2(a). In Fig. 3(a), the trajectories of *flow* starting from various points $(\eta_1, \eta_2) = (\eta_O, 0)$ are also plotted. There are three categories of trajectory according to the value of η_O:

(i) Trajectory for which $(\eta_1, \eta_2) \to (0, -\infty)$ or $(1, \infty)$ as $r \to \infty$ [dashed-dotted line in Fig. 3(a)],

(ii) Periodic trajectory around the middle fixed point $(\eta_b, 0)$ on the η_1 axis [dashed line in Fig. 3(a)],

(iii) Trajectory that reaches $(\eta_a, 0) = (\eta_\infty, 0)$ [solid line in Fig. 3(a)].

The periodic trajectory occurs because of the antisymmetric vector field with respect to η_1 axis. The trajectory that can reach the far-field state is only the (iii)-type and represents a single droplet solution [see the solid line in Fig. 3(c)]. The (iii)-type is the boundary between (i)-type and (ii)-type trajectory families [see Fig. 3(b)], and there is a one to one correspondence between η_O and η_∞ for the (iii)-type. This aspect as the boundary can be observed clearly in Fig. 3(c), where the density distributions for $\eta_O = 0.41865000$ and 0.41864900 are of (i)-type and those for $\eta_O = 0.41864800$ and 0.41864700 are of (ii)-type. The single droplet density distribution is of (iii)-type and the corresponding value of η_O lies between 0.418640800 and 0.41864900 ($\eta_O =$ 0.41864812 up to eight decimal points).

The vector field and *flow* trajectories shown in Fig. 3 do not change if we set $\eta_\infty = 0.287521 (= \eta_b)$ or $\eta_\infty = 0.667059 (= \eta_c)$ in place of $\eta_\infty = 0.1 (= \eta_a)$, since Π remains unchanged (see Sec. IV B). Hence, none of (i)–(iii)-type trajectories reach the far-field state if $\eta_\infty = \eta_b$ or $\eta_\infty = \eta_c$. As is seen from Fig. 2(a), the pair $(\eta_b, \tilde{T}_\infty)$ lies in the unstable region, while $(\eta_c, \tilde{T}_\infty)$ lies in the stable region. Therefore, steady single droplet solutions are not found when the pair of the far-field parameters $(\eta_\infty, \tilde{T}_\infty)$ lies in the unstable or stable region.

As discussed in Sec. IV A, the pair of parameters $(\eta_b, \tilde{T}_\infty)$ always lies in the unstable region. In contrast, $(\eta_a, \tilde{T}_\infty)$ and $(\eta_c, \tilde{T}_\infty)$ lie either in the metastable or stable region. It is numerically verified that if the former lies in the metastable region, the latter in the stable region and vice versa (see Fig. 2). Therefore, if $(\eta_c, \tilde{T}_\infty)$ lies in the metastable region as in Fig. 2(b), then the (iii)-type trajectory flows into the fixed point $(\eta_c, 0)$ and represents a steady single bubble (not droplet) solution. Thus, irrespective of whether a droplet or a bubble, the (iii)-type trajectory is interpreted as the one flowing into a fixed point. When this fixed point is $(\eta_a, 0)$, the trajectory represents a single droplet. When the fixed point is $(\eta_c, 0)$, the trajectory represents a single bubble. Again, when the pair of the far-field parameters lies in the unstable or stable region, single bubble solutions are not found.

Finally, it should be noted that as $(\eta_a, \tilde{T}_\infty)$ approaches $(\eta_G, \tilde{T}_\infty)$ on one branch of the binodal curve, the corresponding $(\eta_c, \tilde{T}_\infty)$ approaches $(\eta_L, \tilde{T}_\infty)$ on the other branch of the binodal curve. In this limit, the (iii)-type trajectory becomes a curve connecting $(\eta_a, 0)$ and $(\eta_c, 0)$ on the $\eta_1\eta_2$ plane.

2. *Cases $D = 2$ and $D = 3$*

Since the first term on the right-hand side remains in Eq. (38b), the vector field is no longer uniform with respect to η_3. Nevertheless, since the η_3 component of the vector field is simple and uniform, we discuss the *flows* by their projection on the $\eta_1\eta_2$ plane for the sake of simplicity. The projection of the trajectory or *flow* will be called the in-plane trajectory or in-plane *flow* in the sequel. As in the case of $D = 1$, three points $(\eta_\alpha, 0)$ $(\alpha = a, b, c)$ on the η_1 axis still remain the fixed points for the in-plane dynamics on the $\eta_1\eta_2$ plane. However, in contrast to the case $D = 1$, the in-plane vector field is no longer antisymmetric with respect to the η_1 axis. This is the influence of the first term on the right-hand side of Eq. (38b). Consequently, periodic trajectories in the case of $D = 1$ are deformed to spiral in-plane trajectories on the $\eta_1\eta_2$ plane. The influence of the first term is larger for larger D. It decreases as η_3 (or r) increases (see Fig. 4).

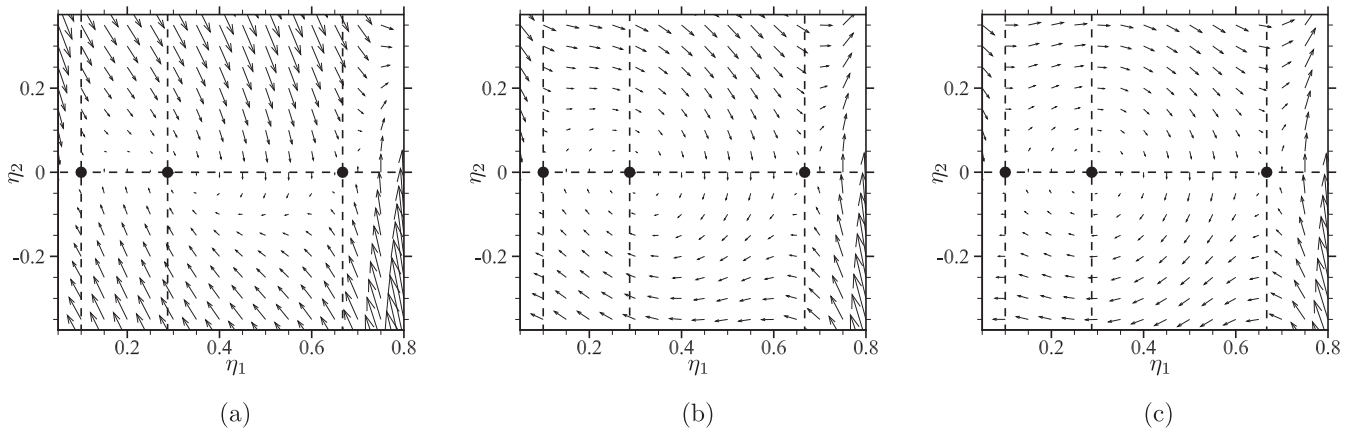

FIG. 4. In-plane vector fields in the case $D = 2$ for $\eta_\infty = 0.1$ and $\tilde{T}_\infty = 0.8$. (a) $\eta_3 = 0.5$. (b) $\eta_3 = 2.0$. (c) $\eta_3 = 100.0$. Closed circles indicate the fixed points $(\eta_\alpha, 0)$ $(\alpha = a, b, c)$ in the $\eta_1\eta_2$ plane.

Figures 5(a) and 5(b) show the in-plane *flow* trajectories in the case $(\eta_\infty, \tilde{T}_\infty) = (0.1, 0.8)$. The case for $D = 1$ is also shown in Fig. 5(c) for reference. The pair of parameters for this figure lies in the metastable region [see Fig. 2(a)]; three zeros of Π, i.e., η_a, η_b, and η_c, are 0.1, 0.287521, and 0.667059, respectively. As is demonstrated in Figs. 5(a) and 5(b), the in-plane trajectories are classified into three, depending on the value of η_O:

(i) In-plane trajectory for which $(\eta_1, \eta_2) \to (0, -\infty)$ or $(1, \infty)$ as $r \to \infty$,

(ii) Spiral in-plane trajectory that flows into $(\eta_b, 0)$ [31],

(iii) In-plane trajectory that flows into $(\eta_a, 0)$.

Since $\eta_\infty = \eta_a$ in Fig. 5, the (iii)-type in-plane trajectory represents a steady single droplet. When η_∞ coincides with other zeros, i.e., $\eta_\infty = 0.287521 (= \eta_b)$ or $\eta_\infty = 0.667059 (= \eta_c)$, the same vector field and trajectories are obtained, since $\Pi(\eta)$ remains unchanged (see Sec. IV B). Hence, as in the case $D = 1$, the *flow* to the far-field condition cannot be found for the pair $(\eta_\infty, \tilde{T}_\infty) = (\eta_c, \tilde{T}_\infty)$ that is in the stable region. However, the *flows* to the far-field condition are possible for the pair $(\eta_\infty, \tilde{T}_\infty) = (\eta_b, \tilde{T}_\infty)$ that is in the unstable region. This is a new type of admissible solution that is not found in the case $D = 1$.

As is mentioned in Sec. IV C 1, the pair $(\eta_b, \tilde{T}_\infty)$ is always in the unstable region, while $(\eta_a, \tilde{T}_\infty)$ and $(\eta_c, \tilde{T}_\infty)$ are either in the metastable and the stable region. Hence, when $(\eta_c, \tilde{T}_\infty)$ is in the metastable region [see Fig. 2(b)], the (iii)-type in-plane trajectory flows into the fixed point $(\eta_c, 0)$ and represents a single bubble. Figure 6 shows such an example. Therefore, the (iii)-type in-plane trajectory flows into a fixed point $(\eta_a, 0)$ [or $(\eta_c, 0)$] and represents a single droplet (or bubble), provided that $(\eta_a, \tilde{T}_\infty)$ [or $(\eta_c, \tilde{T}_\infty)$] lies in the metastable region.

To summarize, the (iii)-type in-plane trajectory that is consistent with the far-field condition is found for $D = 2$ and 3, as in the case $D = 1$, provided that the pair of parameters of far-field condition lies in the metastable region. This type of trajectory represents a single droplet or bubble, depending on whether $\eta_\infty = \eta_a$ or $\eta_\infty = \eta_c$. In addition, the (ii)-type in-plane trajectory is newly found to be consistent with the far-field condition in the unstable region. The properties of these solutions for $D = 2$ and 3 will be further discussed in Sec. IV D.

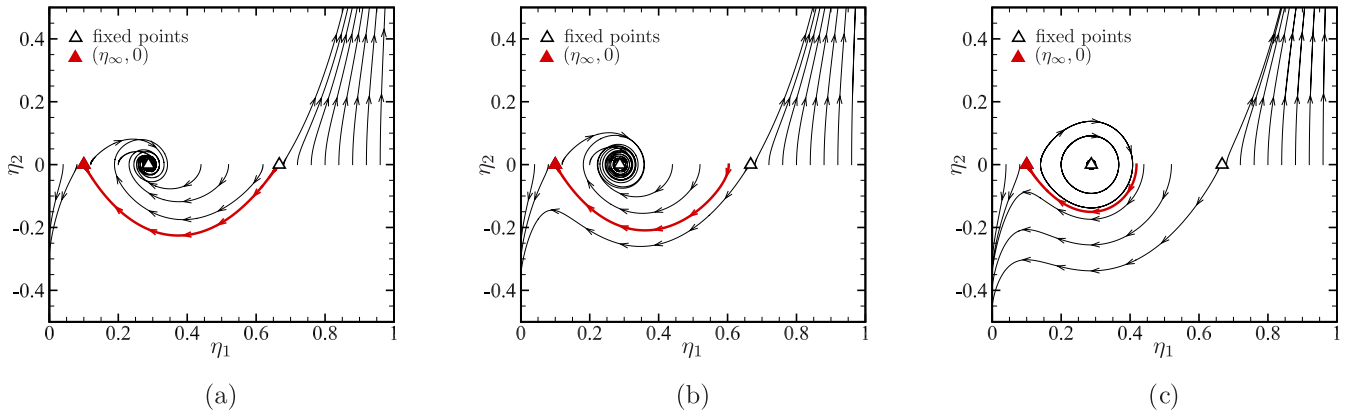

FIG. 5. In-plane trajectories starting from various values of η_O on the η_1 axis for $\eta_\infty = 0.1$ and $\tilde{T}_\infty = 0.8$. (a) $D = 3$. (b) $D = 2$. (c) $D = 1$. Thick line (red) is the in-plane trajectory of a single droplet and ends at a point representing the far-field condition [closed triangle (red)]. Open triangle: the fixed point in the $\eta_1\eta_2$ plane. Closed triangle (red): the point $(\eta_\infty, 0)$ that represents the far-field condition.

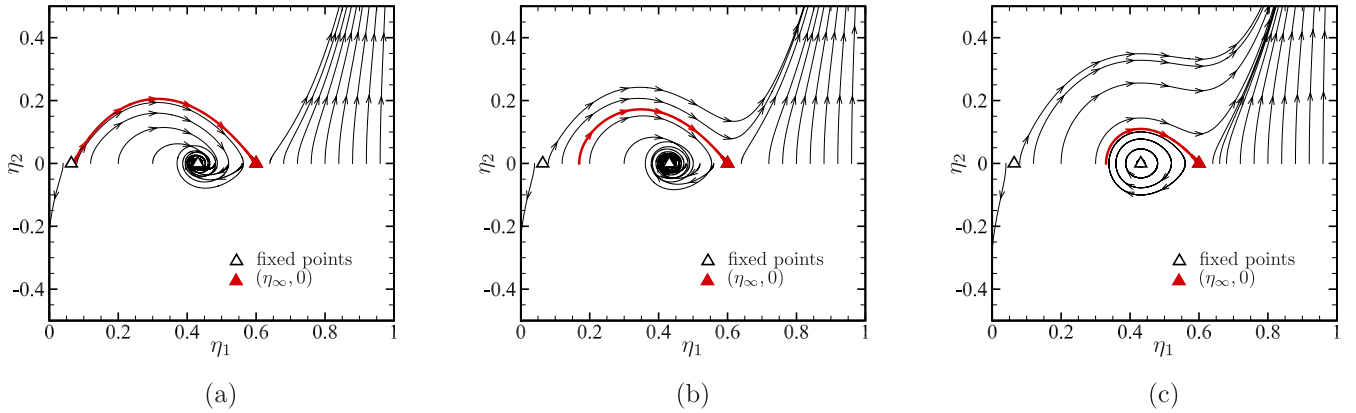

FIG. 6. In-plane trajectories starting from various values of η_O on the η_1 axis for $\eta_\infty = 0.6$ and $\tilde{T}_\infty = 0.8$. See the caption of Fig. 5. (a) $D = 3$. (b) $D = 2$. (c) $D = 1$.

D. Discussions

1. Property of solution in the unstable region

As noted in Sec. IV A, when $(\eta_\infty, \tilde{T}_\infty)$ lies in the unstable region, $\eta_b = \eta_\infty$. In this case, a single droplet (or bubble) solution was not found for $D = 1$. However, for $D = 2$ and 3, the (ii)-type in-plane trajectories are found to represent a solution that satisfies the far-field condition, i.e., $\eta \to \eta_\infty$ as $r \to \infty$. Figure 7 shows an example of such a solution in the case $\eta_O = 0.2$, $\eta_\infty = 0.4$, and $\tilde{T}_\infty = 0.8$. The dimensionless density η is rippled around its far-field value η_∞ with damping the amplitude as r increases. The damping process is very slow and looks dependent on the spatial dimension D. To evaluate the damping behavior in the far field, Taylor expansion is used around η_∞ to transform Eq. (31a) to the equation for the perturbation part $\bar{\eta} = \eta - \eta_\infty$. Taking into account $\Pi(\eta_\infty) = 0$, Eq. (31a) is reduced to

$$\frac{d^2\bar{\eta}}{dr^2} + \frac{D-1}{r}\frac{d\bar{\eta}}{dr} - \Pi'(\eta_\infty)\bar{\eta} = O(\bar{\eta}^2). \tag{41}$$

Note that $\Pi'(\eta_\infty) < 0$ (see Sec. IV A). By setting $z = [-\Pi'(\eta_\infty)]^{1/2} r$ and dropping $O(\bar{\eta}^2)$ term, an approximate equation of Eq. (41) is obtained and read

$$\frac{d^2\bar{\eta}}{dz^2} + \frac{D-1}{z}\frac{d\bar{\eta}}{dz} + \bar{\eta} = 0. \tag{42}$$

The solution of Eq. (42) can be expressed by the Bessel functions, $J_0(z)$ and $Y_0(z)$, of the first and the second kind of order 0 for $D = 2$ and by the spherical Bessel functions, $j_0(z)$ and $y_0(z)$, of the first and the second kind of order 0 for $D = 3$. For large z, it is well known that J_0 and Y_0 decay with the rate $z^{-1/2}$, while j_0 and y_0 decay with the rate z^{-1} (see, e.g., Sec. 9.2 of Ref. [32]). Hence, the observed ripple of density can be estimated to decay with the same rate and η approaches η_∞ as $z \to \infty$. Indeed, the solution of Eq. (31a) is well fitted by the approximate solution $\bar{\eta} + \eta_\infty$ obtained from Eq. (42), see Fig. 7. As is clear in this figure, the influence of $O(\bar{\eta}^2)$ term is small even near the origin, and the approximation (42) well reproduces the solution of Eq. (31a) in the entire domain.

Because of the slow decay of the ripple of density, the solution above may affect the far field and might lose the physical meaning as a single droplet or bubble. Fortunately, however, it is not so. To evaluate the average deviation from

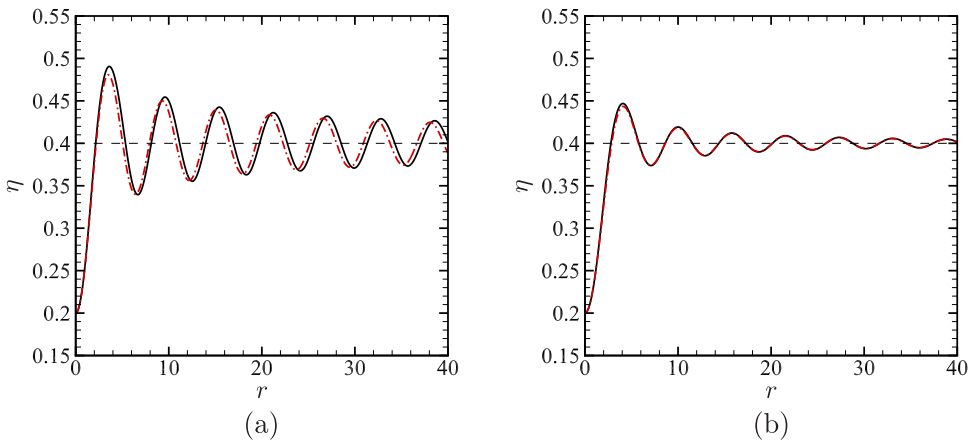

FIG. 7. Radial density distribution for the (ii)-type in-plane trajectory in the unstable region in the case $\eta_O = 0.2$, $\eta_\infty = 0.4$, and $\tilde{T}_\infty = 0.8$. (a) $D = 2$. (b) $D = 3$. Solid line: solution of Eq. (38) that satisfies both conditions (39) and (40). Dashed-dotted line (red): $\bar{\eta} + \eta_\infty$ by the approximation (42) for the corresponding conditions. In panel (b), the deviation of lines is barely visible.

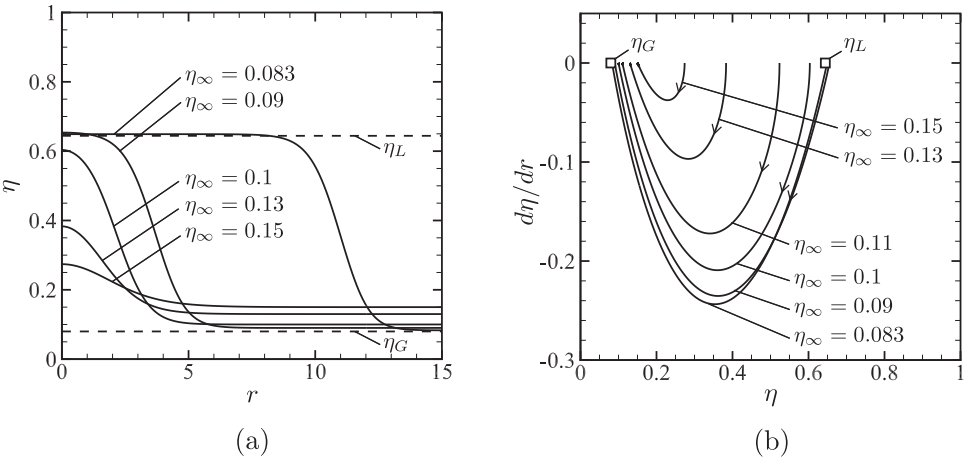

FIG. 8. Radial density distributions and corresponding (iii)-type in-plane trajectories of single droplets for $\tilde{T}_\infty = 0.8$ in the case $D = 2$. (a) Radial density distribution. (b) In-plane trajectory. In panel (b), the arrows indicate the directions of *flow* on the individual trajectories and open squares indicate the values on the liquid-side branch η_L and the gas-side branch η_G of the binodal curve at $\tilde{T}_\infty = 0.8$.

η_∞ caused by the solution, consider the quantity

$$(D/Z^D)\int_0^Z z^{D-1}\bar{\eta}(z)dz, \tag{43}$$

replace $\bar{\eta}$ by J_0 and Y_0 for $D = 2$ (or j_0 and y_0 for $D = 3$), and take the limit as $Z \to \infty$. Then, the result is found to be zero. Namely, the solution does not affect the average density in the whole domain and thus η_∞ is not affected. In this sense, the (ii)-type in-plane trajectory for $\eta_\infty = \eta_b$ makes sense as a solution for a single droplet or bubble in the case $D = 2$ or 3. Additional side evidence is presented in the Appendix B.

2. *Property of solution in the metastable region*

When $\eta_\infty = \eta_a$ or η_c, the trajectories that satisfy the far-field condition were found, irrespective of the spatial dimension. Figures 8 and 9 show various radial density distributions and corresponding in-plane trajectories when varying η_∞ within the metastable region for $\tilde{T}_\infty = 0.8$ in the case $D = 2$. The density changes monotonically with respect to r. In Fig. 8 the radius of droplet increases with decreasing η_∞, while in Fig. 9 the radius of bubble increases with increasing η_∞. In both cases, as the radius increases, the density ratio between two phases increases and tends to saturate in such a way that the pair of η_O and η_∞ approaches the pair of values $\eta_L(\tilde{T}_\infty)$ and $\eta_G(\tilde{T}_\infty)$ on the binodal curve. Since $\Pi(\eta_O) = \Pi(\eta_\infty) = 0$ on the binodal curve (36), the corresponding radial density distribution from η_O to η_∞ is the one represented by the in-plane trajectory that connects two fixed points $(\eta_a, 0)$ and $(\eta_c, 0)$. This provides an interpretation of the density distribution for the pair of parameters on the binodal curve in light of the *flow* in phase space.

In the meantime, if $\Pi(\eta_O) \neq 0$, then $d^2\eta/dr^2 \neq 0$ at the origin by Eq. (31a). It implies that the interior of droplet or bubble with such a η_O is not sufficiently uniform and that the Young–Laplace (YL) relation [22,33] may be broken.

The YL relation is the condition of mechanical balance on the Gibbs surface that is a discontinuous boundary model between uniform two phases with different density [22]. Denoting the radius of the Gibbs surface (Gibbs radius, for short) by $\mathcal{R}_\mathrm{I}$, the inside uniform pressure by p_O, the outside uniform pressure by p_∞, and the surface tension of the interface by γ,

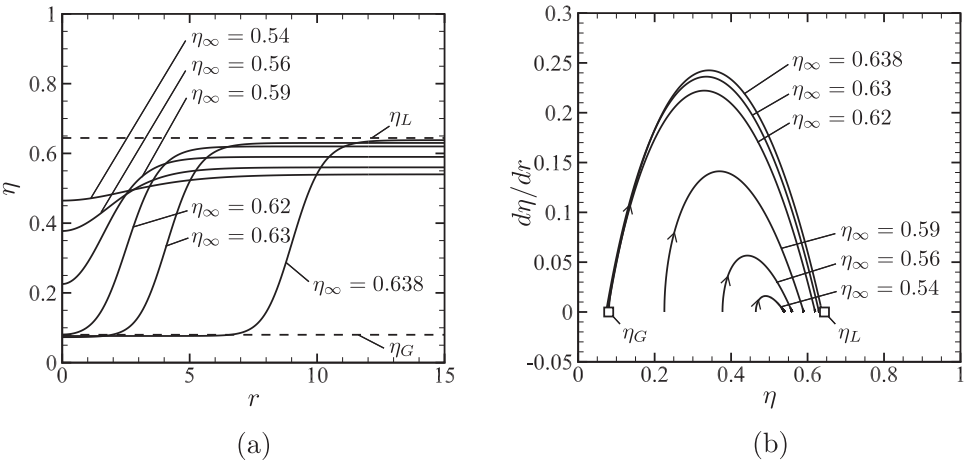

FIG. 9. Radial density distributions and corresponding (iii)-type in-plane trajectories of single bubbles for $\tilde{T}_\infty = 0.8$ in the case $D = 2$. See the caption of Fig. 8.

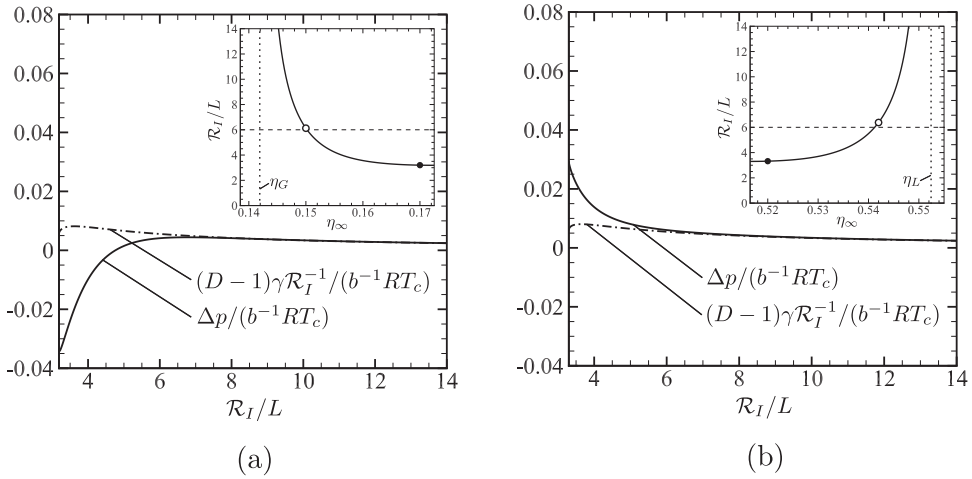

FIG. 10. Dependence of pressure difference Δp between inside and outside of droplet (or bubble) and the corresponding surface tension γ on the Gibbs radius $\mathcal{R}_I$ for $\tilde{T}_\infty = 0.9$ in the case $D = 2$. (a) Droplet. (b) Bubble. Solid line: pressure difference. Dashed-dotted line: surface tension divided by $\mathcal{R}_\mathrm{I}$. Deviation between the lines indicate the breakdown of the Young–Laplace relation (44). The upper-right plot in each panel is η_∞ vs $\mathcal{R}_\mathrm{I}$. The open and closed circles indicate the cases for which the simulations to be shown in Figs. 12–15 have been conducted.

the mechanical balance condition is written as

$$\Delta p \equiv p(\eta_\infty, \tilde{T}_\infty) - p(\eta_O, \tilde{T}_\infty) = \frac{(D-1)\gamma}{\mathcal{R}_\mathrm{I}}. \tag{44}$$

On the one hand, since the Gibbs surface is defined under a constraint of the total mass in the system, the Gibbs radius $\mathcal{R}_\mathrm{I}$ is determined by the relation

$$\int (\rho - \rho_\infty) d\boldsymbol{X} = \frac{\pi}{2D}(2\mathcal{R}_\mathrm{I})^D(\rho_O - \rho_\infty). \tag{45}$$

On the other hand, since the surface tension is defined by the free energy associated with the interface per unit area, appropriate consideration of the free energy is necessary. Fortunately, it can be done along the same line as in Ref. [11] and the free energy $\mathcal{H}$ of the system relative to the far-field uniform state is given by

$$\mathcal{H} = \frac{1}{RT_\infty}\int \left(\rho\mathcal{F}(\rho) - \rho_\infty\mathcal{F}(\rho_\infty) + \frac{\kappa}{2}\left(\frac{\partial\rho}{\partial X_i}\right)^2\right) d\boldsymbol{X}, \tag{46}$$

$$\begin{aligned}\mathcal{F}(\rho) &= \left(\ln\frac{b\rho}{1-b\rho} + \frac{3}{2}\right)RT_\infty - a\rho + \text{const.} \\ &= RT_c\Pi(\eta) - \frac{p}{\rho} + \text{const.},\end{aligned} \tag{47}$$

in the case that the VDF is a resting Maxwellian with temperature T_∞. Under the ansatz of the Gibbs surface, $\mathcal{H}$ is expressed with the aid of the interface free energy $\mathcal{I}$ as

$$\mathcal{H} = \frac{\pi}{2D}\frac{(2\mathcal{R}_\mathrm{I})^D}{RT_\infty}[\rho_O\mathcal{F}(\rho_O) - \rho_\infty\mathcal{F}(\rho_\infty)] + \frac{\mathcal{I}}{RT_\infty}. \tag{48}$$

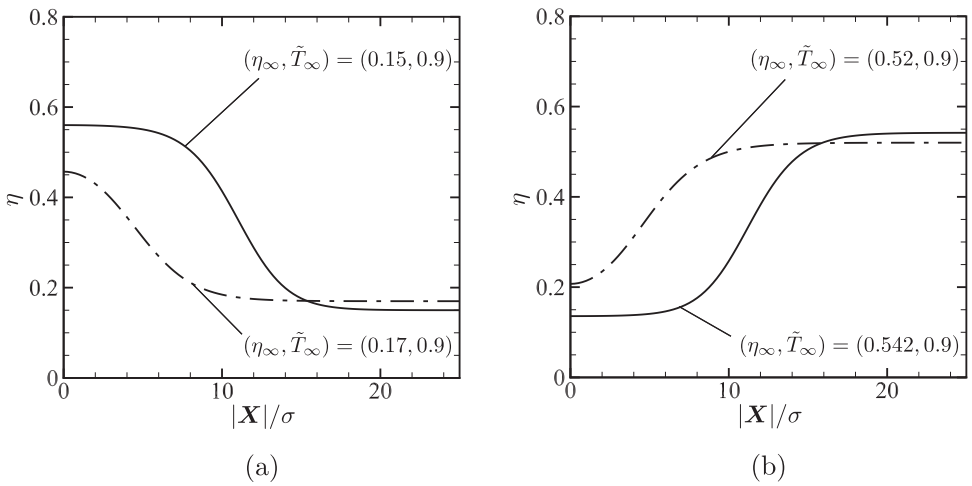

FIG. 11. Radial density distribution of droplets and bubbles for stability assessment ($\tilde{T}_\infty = 0.9$ and $D = 2$). (a) Droplets. (b) Bubbles. Solid lines are the cases shown by open circles in Fig. 10, while dashed-dotted lines are those shown by closed circles in Fig. 10.

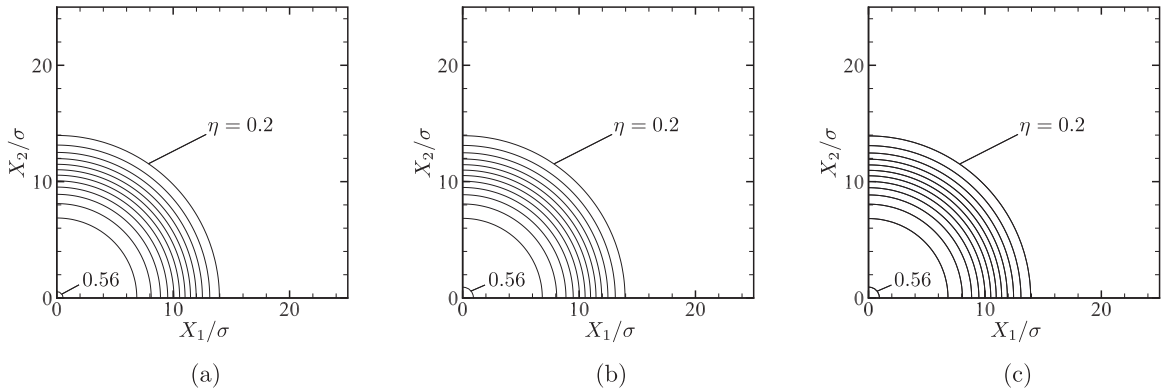

FIG. 12. Simulation of stability for the droplet with the radial density distribution indicated by the solid line in Fig. 11(a), i.e., the case $(\eta_\infty, \tilde{T}_\infty) = (0.15, 0.9)$ and $D = 2$. Contours of $\eta(=b\rho) = 0.2 + 0.03m$ $(m = 0, 1, \dots)$ are plotted. (a) $t/t_c = 0$. (b) $t/t_c = 3000$. (c) $t/t_c = 5000$.

Since the surface tension γ is $\mathcal{I}$ divided by the surface area $(2\mathcal{R}_\mathrm{I})^{D-1}\pi$, it is expressed by Eqs. (46) and (48) as

$$\gamma = \frac{\mathcal{H}RT_\infty}{(2\mathcal{R}_\mathrm{I})^{D-1}\pi} + \frac{\mathcal{R}_\mathrm{I}}{D}[\rho_\infty \mathcal{F}(\rho_\infty) - \rho_O \mathcal{F}(\rho_O)]. \tag{49}$$

Figure 10 plots Δp and $\gamma/\mathcal{R}_\mathrm{I}$, obtained separately, against the Gibbs radius $\mathcal{R}_\mathrm{I}$ in the case $D = 2$. As a reference, $\mathcal{R}_\mathrm{I}$ versus η_∞ is also shown in the upper right corner of each panel. It is seen that, as η_∞ becomes closer to η_L or η_G (the values on the binodal curve), the Gibbs radius $\mathcal{R}_\mathrm{I}$ becomes larger [34] and the violation of the YL relation becomes smaller. However, if η_∞ is away from η_L or η_G so that $\mathcal{R}_\mathrm{I}/L \lesssim 6$, then the YL relation is violated, which supports the expectation stated at the end of the second paragraph of Sec. IV D 2. The criterion in the case $D = 3$ is almost the same, i.e., $\mathcal{R}_\mathrm{I}/L \lesssim 6$, which is omitted here.

V. STABILITY OF SINGLE DROPLET OR BUBBLE

To assess the stability of (ii)-type and (iii)-type steady solutions, direct numerical simulations of Eq. (1) have been conducted with the resting Maxwellian (23) being the initial condition and with $\kappa = a\sigma^2$ [35] in the case $D = 2$. The density of the initial Maxwellian is the one obtained through the study in Secs. III and IV. The numerical computations are conducted by first eliminating the ξ_3 dependence from Eq. (1) by using Chu's method [36] in a finite spatial and molecular velocity domain truncated as $|X_1|, |X_2| \leqslant L_d$ and $|\xi_1|, |\xi_2| \leqslant 6\sqrt{2RT_c}$. The partial elimination of the velocity variable is the benefit of using model equation over the Enskog–Vlasov equation, which is the standard technique in the literature of rarefied gas dynamics; see, e.g., Ref. [37]. The VDF is assumed to be zero outside of the truncated domain of molecular velocity, while it is assumed to be kept at the initial Maxwellian outside of the truncated spatial domain. Only the first quadrant of space $0 \leqslant X_1, X_2 \leqslant L_d$ is treated by assuming the mirror symmetry with respect to $X_1 = 0$ and $X_2 = 0$. The numerical scheme is based on the semi-Lagrangian and Strang splitting method [38–40] and a uniform time step $0.02t_c$ is used, where $t_c = \sigma/\sqrt{2RT_c}$ is the reference time. The stability is assessed by observing whether the initial Maxwellian is maintained for a long time. The collapse of unstable droplet or bubble is induced only by the numerical errors caused by the discretization, interpolations, etc., in such simple assessment. Thus, only the linearly unstable droplet or bubble can be detected. Stability against large fluctuations, for instance, is not within the scope of the present simulations. Since the process of collapse depends on those errors, numerical

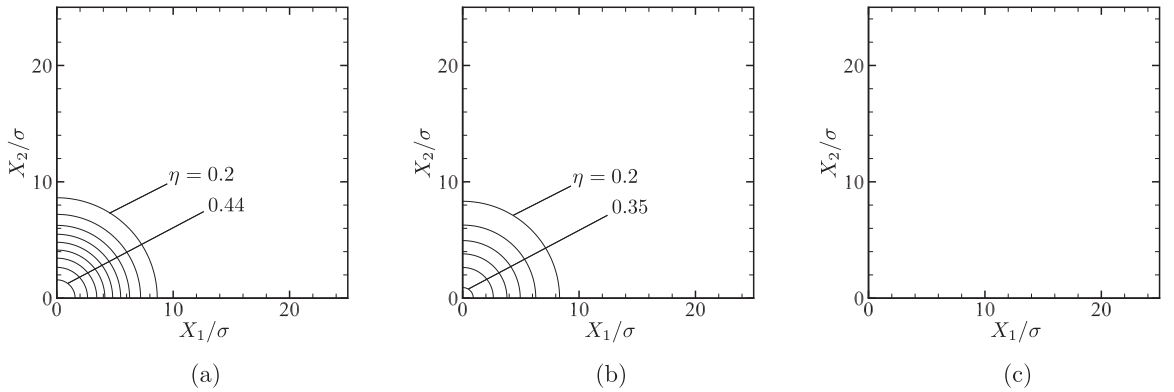

FIG. 13. Simulation of stability for the droplet with the radial density distribution indicated by the dashed-dotted line in Fig. 11(a), i.e., the case $(\eta_\infty, \tilde{T}_\infty) = (0.17, 0.9)$ and $D = 2$. Contours of $\eta(=b\rho) = 0.2 + 0.03m$ $(m = 0, 1, \dots)$ are plotted. (a) $t/t_c = 0$. (b) $t/t_c = 3000$. (c) $t/t_c = 5000$. In panel (c), $0.17 < \eta < 0.173$ entirely and no contour is plotted accordingly.

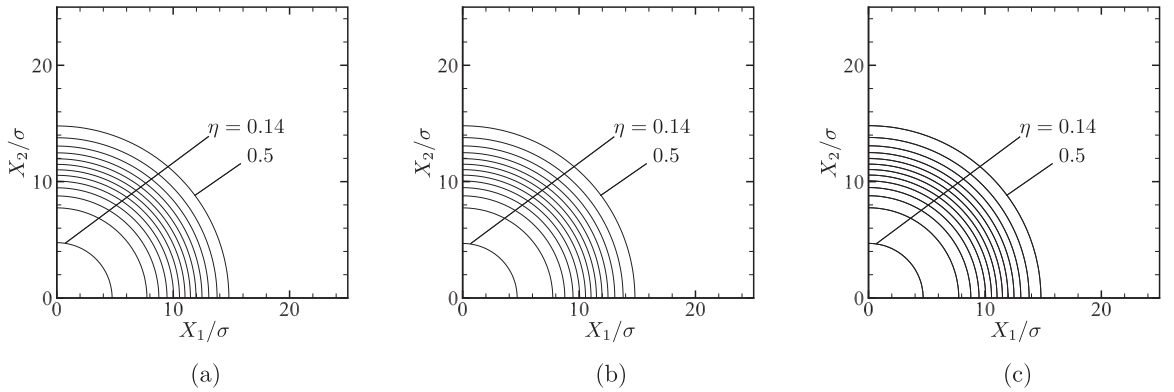

FIG. 14. Simulation of stability for the bubble with the radial density distribution indicated by the solid line in Fig. 11(b), i.e., the case $(\eta_\infty, \tilde{T}_\infty) = (0.542, 0.9)$ and $D = 2$. Contours of $\eta(=b\rho) = 0.5 - 0.03m$ $(m = 0, 1, \dots)$ are plotted. (a) $t/t_c = 0$. (b) $t/t_c = 500$. (c) $t/t_c = 1000$.

convergence with respect to the discrete resolution or the size of the truncated spatial domain was not aimed at in the present simulations.

A. Single droplet or bubble in the metastable region

As a stability test of the solution in the metastable region, simulations are conducted for the single droplets with the radial density distributions shown in Fig. 11(a) in the case $D = 2$. The far-field parameters are $(\eta_\infty, \tilde{T}_\infty) = (0.15, 0.9)$ and $(0.17, 0.9)$, respectively. The corresponding Gibbs radius is larger for the former; see open and closed circles in Fig. 10(a). Figures 12 and 13 show the results obtained by setting $L_d/\sigma = 50$ with 200×200 uniform divisions in the quadrant $0 \leqslant X_1, X_2 \leqslant L_d$ and 128×128 uniform divisions in molecular velocity. The droplet is maintained in the long time evolution for the case $(\eta_\infty, \tilde{T}_\infty) = (0.15, 0.9)$ where the corresponding Gibbs radius is larger, while it collapses for the case $(\eta_\infty, \tilde{T}_\infty) = (0.17, 0.9)$ where the corresponding Gibbs radius is smaller.

The difference of stability with respect to the Gibbs radius is also observed in the case of bubbles. Figures 14 and 15 show the results for the bubbles with the radial density distributions shown in Fig. 11(b) in the case $D = 2$. The computational parameters are the same as those used in the droplet cases in Figs. 12 and 13. Again, the bubble is maintained for a long time in the case $(\eta_\infty, \tilde{T}_\infty) = (0.542, 0.9)$ where the corresponding Gibbs radius is larger, while it collapses in the case $(\eta_\infty, \tilde{T}_\infty) = (0.52, 0.9)$ where the corresponding Gibbs radius is smaller; see the open and closed circles in Fig. 10(b).

Irrespective of whether droplet or bubble, the pair of far-field parameters for the steady single droplet or bubble lies near the binodal curve in the metastable region. It is thus suggested that single stable droplets or bubbles are formed only near the binodal curve in the metastable region.

Finally, it should be noted that both droplet and bubble collapse in the case of closed circles in Fig. 10, while they are maintained for a long time in the case of open circle in Fig. 10. Since the YL relation breaks down for closed circles in Fig. 10 and is still valid for open circles, it is strongly suggested that the YL relation holds for stable single droplet or bubble. Indeed, MD simulation results in the literature such as Refs. [5,6] have reported the generation of nano-sized bubbles, further confirming the validity of the YL relation for those bubbles. At the same time, Ref. [5] has reported difficulties in keeping much smaller bubbles for a long time.

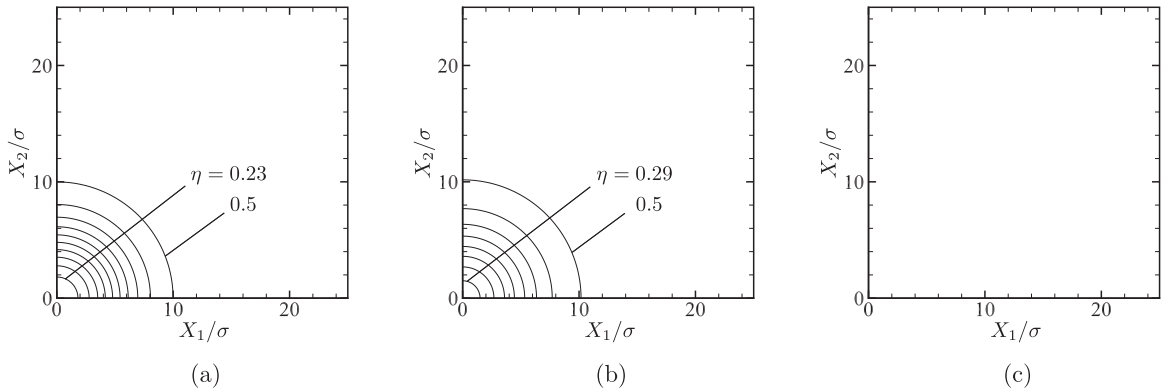

FIG. 15. Simulation of stability for the bubble with the radial density distribution indicated by the dashed-dotted line in Fig. 11(b), i.e., the case $(\eta_\infty, \tilde{T}_\infty) = (0.52, 0.9)$ and $D = 2$. Contours of $\eta(= b\rho) = 0.5 - 0.03m$ $(m = 0, 1, \dots)$ are plotted. (a) $t/t_c = 0$. (b) $t/t_c = 500$. (c) $t/t_c = 1000$. In panel (c), $0.500 < \eta < 0.52$ entirely and no contour is plotted accordingly.

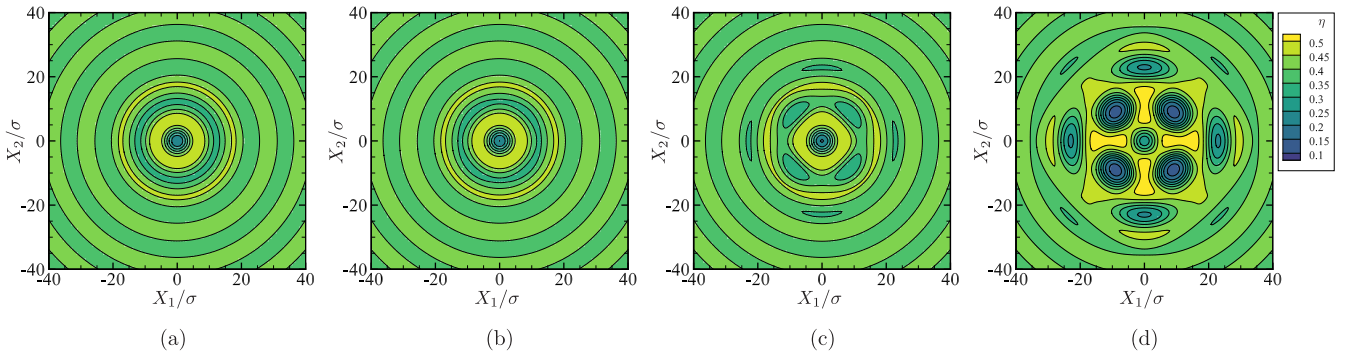

FIG. 16. Simulation for the collapse of the solution in the unstable region with the radial density distribution indicated by the solid line in Fig. 7(a): $(\eta_O, \eta_\infty, \tilde{T}_\infty) = (0.2, 0.4, 0.8)$ in the case $D = 2$. Contour plots of $\eta(=b\rho)$ are shown. (a) $t/t_c = 0$. (b) $t/t_c = 100$. (c) $t/t_c = 150$. (d) $t/t_c = 200$.

Note that there are no terms representing fluctuations in our one-particle distribution model (1a). Nevertheless, the above observations are consistent with the MD simulation results. The trigger of the collapse in the present simulations is the numerical errors occurring in the discretization and approximation procedure. Therefore, the detected collapse is not related to the type of fluctuations, but rather to the structure of the droplet or bubble itself. Our dynamical system approach combined with the numerical simulations enables us to make clear this point, since unstable droplet or bubble cannot be obtained by the MD approach with fluctuations.

B. Single droplet or bubble in the unstable region

As a stability test of the solution in the unstable region, simulations are conducted for the solution with the radial density distributions shown in Fig. 7(a) in the case $D = 2$. The set of origin and far-field parameters is $(\eta_O, \eta_\infty, \tilde{T}_\infty) = (0.2, 0.4, 0.8)$. Figure 16 shows the results obtained by setting $L_d/\sigma = 120$ with 480×480 uniform divisions in the quadrant $0 \leqslant X_1, X_2 \leqslant L_d$ and 192×192 uniform divisions in molecular velocity. This setting offers the highest resolution in discretization and the largest spatial domain (thus the least influence of truncation of space) in the present computational work. Simulations have been performed with other settings as well but they are omitted to report here.

As a whole, the speed of collapse is faster than those observed in the metastable region, see Figs. 13 and 15, suggesting the difficulties to find a stable droplet or bubble of the Bessel (or spherical Bessel) function-type structure shown in Fig. 7. This may be connected with the fact that unstable small droplets or bubbles in the metastable region are found closer to the spinodal than to the binodal curve. However, the process of collapse is more complicated in the unstable region and induces new centers of many droplets and bubbles. This feature looks supporting the scenario of spinodal decomposition in the literature (see also Appendix B).

VI. CONCLUSION

In the present paper, we have discussed the steady single droplet or bubble and its stability on the basis of the kinetic model equation proposed in Ref. [19]. After the presentation of kinetic model in Sec. II, the problem is reduced to a problem of the radial density distribution, assuming the resting Maxwellian with a uniform temperature and isotropic field with respect to the origin of the coordinates in Sec. III. The reduced problem is treated as a low-dimensional dynamical system in Sec. IV and is studied by using the concept of the phase space vector field, fixed point, and *flow*. The trajectories in phase space are found to change qualitatively whether the set of parameters of the far-field uniform state falls into the unstable region or the metastable region. In particular, the structure of the single droplet or bubble in the unstable region is found to be well described by the family of the Bessel and the spherical Bessel functions for spatially two- and three-dimensional cases. In the metastable region, the droplet or bubble is always of a radially monotone structure in density. Its inside is not necessarily at a fully developed uniform state, and accordingly the YL relation may be broken in such a case.

The stability of thus obtained steady single droplet or bubble is also tested numerically by a simple assessment. The results suggest that the single droplet or bubble becomes unstable away from the binodal curve in the metastable region. This is consistent with the MD simulation results in the literature. Since there are no terms representing fluctuations in our one-particle distribution model, the observed instability is due to the structure of the droplet or bubble itself. We have discussed this feature in view of the YL relation and the size of droplet or bubble. The process of collapse of the droplet or bubble, in particular the difference of qualitative features in the metastable and the unstable region, is also demonstrated.

ACKNOWLEDGMENTS

The present work has been partially supported by HPCI and JHPCN system Research Projects No. hp210007, No. hp220077, No. hp230028, and No. jh240005, by the JSPS KAKENHI Grants No. 17K18840 and No. 22K03923, and by grants from the Mori Manufacturing Research and Technology Foundation to T.M. and from the Kyoto University Foundation to S.T. T.M. thanks Livio Gibelli for the hospitality and discussion during his stay in the University of Edinburgh that was financially supported by the Mazume grant. The authors also thank Shugo Yasuda and Hayato Shiba for their advices and the Center for Cooperative Work on Data science and Computational science, University of Hyogo for the use of the facilities, in

developing a GPU code by which a part of simulations have been conducted.

APPENDIX A: MAXWELLIAN AS A TIME ASYMPTOTIC SOLUTION

In this Appendix, we will show that, under suitable assumptions at a far distance, there is a functional monotonically decreasing in time and that the solution of Eq. (1) approaches a local resting Maxwellian with uniform temperature T_∞. This feature is one of the chief merits of our kinetic model over the original Enskog–Vlasov equation.

Consider the problem (1). Let us denote the uniform resting Maxwellian and Φ_S at a far distance by f_∞ and $\Phi_{S\infty}$, respectively. We first integrate Eq. (1a) multiplied by $\ln(f/f_\infty) - \Phi_{S\infty}/(RT_\infty)$ with respect to $\boldsymbol{\xi}$ and then further integrate the resulting with respect to $\boldsymbol{X}$ over a control volume $\mathcal{D}$, where $\mathcal{D}$ is the spherical domain centered at the origin with a sufficiently large radius $\mathcal{R}_d$. After some manipulations [11,19], we obtain

$$\begin{aligned}\frac{d}{dt}\int_{\mathcal{D}}(H[f]-H[f_\infty])d\boldsymbol{X} &= \int_{\partial\mathcal{D}}\int \xi_i n_i f\left(\ln\frac{f}{f_\infty}-1\right)d\boldsymbol{\xi}dS \\ &+ \int_{\partial\mathcal{D}} H_i[f]n_i dS + \int_{\mathcal{D}}\left\{\int\left(\ln\frac{f}{f_\infty}\right)Q_c^\flat[f]d\boldsymbol{\xi}\right. \\ &- \frac{\lambda_P}{RT^2}\left(\frac{\partial T}{\partial X_k}\right)^2 - \frac{\mu_P}{2RT}\left(\overline{\frac{\partial v_i}{\partial X_j}}\right)^2 \\ &\left.- \frac{\mu_B}{RT}\left(\frac{\partial v_k}{\partial X_k}\right)^2\right\}d\boldsymbol{X}, \end{aligned} \tag{A1a}$$

where n_i is the inward normal unit to the surface $\partial\mathcal{D}$ and

$$\begin{aligned}H[f] &= \int f\left(\ln\frac{f}{f_\infty}-1\right)d\boldsymbol{\xi} + \frac{T_\infty - T}{RT_\infty}\int\frac{\partial\Phi_S}{\partial T}d\rho \\ &+ \frac{1}{RT_\infty}\left(\rho(\Phi_S-\Phi_{S\infty}) - \int\rho\frac{\partial\Phi_S}{\partial\rho}d\rho\right) \\ &+ \frac{\kappa}{2RT_\infty}\left(\frac{\partial\rho}{\partial X_k}\right)^2, \end{aligned} \tag{A1b}$$

$$\begin{aligned}H_i[f] =& \frac{v_i}{RT_\infty}\left[(T_\infty - T)\int\frac{\partial\Phi_S}{\partial T}d\rho - \rho(\Phi_S - \Phi_{S\infty} + \Phi_L)\right] \\ &- \frac{v_j}{RT_\infty}\left(\mu_P\overline{\frac{\partial v_i}{\partial X_j}} + \mu_B\frac{\partial v_k}{\partial X_k}\delta_{ij}\right) \\ &- \frac{T-T_\infty}{RTT_\infty}\lambda_P\frac{\partial T}{\partial X_i} + \frac{\kappa}{RT_\infty}\frac{\partial\rho v_k}{\partial X_k}\frac{\partial\rho}{\partial X_i}. \end{aligned} \tag{A1c}$$

Note that the constant $H[f_\infty]$ is subtracted from $H[f]$ in Eq. (A1a) to avoid the integral diverging in the limit $\mathcal{R}_d \to \infty$. Thanks to the property of $Q_c^\flat$ [24], all the four terms in the last integral on the right-hand side of Eq. (A1a) are nonpositive, and thus the following inequality holds:

$$\begin{aligned}\frac{d}{dt}\int_{\mathcal{D}}(H[f]-H[f_\infty])d\boldsymbol{X} \leqslant& \int_{\partial\mathcal{D}} H_i[f]n_i dS \\ &+ \int_{\partial\mathcal{D}}\int\xi_i n_i f\left(\ln\frac{f}{f_\infty}-1\right)d\boldsymbol{\xi}dS, \end{aligned} \tag{A2}$$

where the equality holds if and only if f is a Maxwellian with uniform T and v_i. By the far-field condition (1b), these uniform T and v_i ought to be T_∞ and zero, respectively.

To evaluate each term on the right-hand side of Eq. (A2), we will make two reasonable assumptions: (i) the net mass flux and the net heat flux on the control surface are finite, so that the mass flow and heat flow normal to the surface decays at most with the rate of $|\boldsymbol{X}|^{-2}$ at a far distance. Moreover, we further assume that mass and heat flow are also at the same order, since the far field is a given resting uniform Maxwellian; (ii) because of (i), the deviation of f from f_∞ is expected to vanish very slowly ($\sim|\boldsymbol{X}|^{-m}$ with m being some positive number), which implies that the length scale of change around the control surface $\partial\mathcal{D}$ is $\mathcal{R}_d$ and thus the effective Knudsen number there defined by the ratio of the reference mean-free-path $\ell_\infty = (2RT_\infty)^{1/2}/A_\infty^\flat$, where $A_\infty^\flat = A^\flat(\rho_\infty, T_\infty)$, to the scale length $\mathcal{R}_d$ is small, i.e., $\epsilon \equiv \ell_\infty/\mathcal{R}_d \ll 1$ [41]. Therefore, the VDF around the control surface can be well evaluated by the Chapman–Enskog (CE) expansion.

Under these reasonable assumptions, we can show that

$$\lim_{\mathcal{R}_d\to\infty}\int_{\partial\mathcal{D}} H_i[f]n_i dS = 0, \tag{A3}$$

$$\lim_{\mathcal{R}_d\to\infty}\int_{\partial\mathcal{D}}\int\xi_i n_i f\left(\ln\frac{f}{f_\infty}-1\right)d\boldsymbol{\xi}dS = 0. \tag{A4}$$

To prove Eq. (A3), first consider Eq. (A1c). Keeping in mind that the heat flow at a far distance is well described by the gradient of temperature, the first term on the right-hand side of Eq. (A2) can be well evaluated by the assumption (i). Indeed, since $v_i \sim |\boldsymbol{X}|^{-2}$ and $q_i(\propto \partial T/\partial X_i) \sim |\boldsymbol{X}|^{-2}$, each term on the right-hand side of Eq. (A1c) is estimated as a small quantity multiplied by $|\boldsymbol{X}|^{-2}$, where the small quantity is the one that tends to vanish as $|\boldsymbol{X}| \to \infty$, such as $T_\infty - T$, $\Phi_S - \Phi_{S\infty}$, $\Phi_L(\propto \partial^2\rho/\partial X_i^2)$, $\partial v_i/\partial X_j$, and $\partial\rho/\partial X_i$. Therefore, once integrated over the control surface, the integral of each term multiplied by n_i is estimated as the same size as the small quantity. Hence, each term vanishes in the limit $\mathcal{R}_d \to \infty$, the estimate (A3) is obtained.

Next, to prove Eq. (A4), consider the last term on the right-hand side of Eq. (A2). Compared with the case of Eq. (A3), we need more details about the asymptotic behavior at a far field and thus make use of the CE expansion based on the assumption (ii). We present the outline of the analyses below.

To make clear the ordering in the CE expansion, we use the dimensionless notation

$$\hat{t} = \frac{(2RT_\infty)^{1/2}}{\mathcal{R}_d}t, \quad x_i = \frac{X_i}{\mathcal{R}_d}, \quad \zeta_i = \frac{\xi_i}{(2RT_\infty)^{1/2}},$$

$$\hat{f} = \frac{(2RT_\infty)^{3/2}}{\rho_\infty}f, \quad \hat{F}_i = -\frac{\partial}{\partial x_i}(\hat{\Phi}_S + \hat{\Phi}_L),$$

$$\hat{\Phi}_S = \frac{\Phi_S}{2RT_\infty}, \quad \hat{\Phi}_L = \frac{\Phi_L}{2RT_\infty}, \quad \hat{Q}_c^\flat = \frac{(2RT_\infty)^{3/2}}{\rho_\infty A_\infty^\flat}Q_c^\flat,$$

$$\hat{Q}_d + \epsilon\hat{Q}_d^\flat = \frac{2\mathcal{R}_d RT_\infty}{\rho_\infty} Q_d^\flat, \quad \hat{A}^\flat = \frac{A^\flat}{A_\infty^\flat},$$
$$\hat{\alpha}_i = \frac{\mathcal{R}_d}{2RT_\infty}\alpha_i, \quad \hat{\beta} = \frac{\mathcal{R}_d}{(2RT_\infty)^{1/2}}\beta, \quad \hat{\rho} = \frac{\rho}{\rho_\infty},$$
$$\hat{T} = \frac{T}{T_\infty}, \quad \hat{v}_i = \frac{v_i}{(2RT_\infty)^{1/2}}, \quad \hat{c}_i = \frac{c_i}{(2RT_\infty)^{1/2}},$$
$$\breve{\mu}_P = \frac{A_\infty^\flat \mu_P}{\rho_\infty RT_\infty}, \quad \breve{\mu}_B = \frac{A_\infty^\flat \mu_B}{\rho_\infty RT_\infty}, \quad \breve{\lambda}_P = \frac{A_\infty^\flat}{\rho_\infty RT_\infty}\frac{\lambda_P}{2R},$$

and rewrite Eq. (1a) into

$$\frac{\partial \hat{f}}{\partial \hat{t}} + \zeta_i \frac{\partial \hat{f}}{\partial x_i} + \hat{F}_i \frac{\partial \hat{f}}{\partial \zeta_i} = \frac{1}{\epsilon}\hat{Q}_c^\flat + \hat{Q}_d + \epsilon\hat{Q}_d^\flat. \tag{A5a}$$

Here the original $Q_d^\flat$ has been decomposed into dimensionless $\hat{Q}_d$ and $\hat{Q}_d^\flat$ in such a way that

$$\hat{Q}_d = -\frac{\partial}{\partial \zeta_i}[(\hat{\alpha}_i + \hat{\beta}\hat{c}_i)\hat{f}], \tag{A5b}$$

$$\hat{Q}_d^\flat = -\frac{1}{3\hat{\rho}\hat{T}}\frac{\partial}{\partial \zeta_i}\left(\left\{\frac{3}{2}\hat{T}\frac{\partial \breve{S}_{ij}}{\partial x_j} + \hat{c}_i\left[\frac{\partial}{\partial x_k}\left(\breve{\lambda}_P\frac{\partial \hat{T}}{\partial x_k}\right) + \frac{\partial \hat{v}_j}{\partial x_k}\breve{S}_{jk}\right]\right\}\hat{f}\right), \tag{A5c}$$

$$\breve{S}_{ij} = \breve{\mu}_P\overline{\frac{\partial \hat{v}_i}{\partial x_j}} + \breve{\mu}_B\frac{\partial \hat{v}_k}{\partial x_k}\delta_{ij}. \tag{A5d}$$

By following the standard procedure of the CE expansion, we seek the solution of Eq. (A5a) in the form

$$\hat{f} = \hat{f}^{(0)} + \epsilon\hat{f}^{(1)} + \epsilon^2\hat{f}^{(2)} + \cdots. \tag{A6}$$

The details of the calculation for the present kinetic model can be found in the Appendix of Ref. [19]. Here we summarize the results up to $O(\epsilon)$:

$$\hat{f}^{(0)} = \frac{\hat{\rho}}{(\pi\hat{T})^{3/2}}\exp\left(-\frac{\hat{c}_k^2}{\hat{T}}\right), \tag{A7a}$$

$$\hat{f}^{(1)} = \left(\hat{A}_i\hat{c}_i + \hat{B}\hat{c}_k^2 + \hat{C}_{ij}\hat{c}_i\hat{c}_j + \hat{D}_i\hat{c}_i\hat{c}_k^2\right)\frac{\hat{f}^{(0)}}{\hat{A}^\flat}, \tag{A7b}$$

where $\hat{A}_i$, $\hat{B}$, $\hat{C}_{ij}$, and $\hat{D}_i$ are the following dimensionless version of the quantities to be defined later in Eqs. (A9b)–(A9e):

$$\hat{A}_i = \mathcal{R}_d A_i, \quad \hat{B} = \frac{\mathcal{R}_d}{2}(2RT_\infty)^{1/2}B,$$
$$\hat{C}_{ij} = \frac{\mathcal{R}_d}{2}(2RT_\infty)^{1/2}C_{ij}, \quad \hat{D}_i = \mathcal{R}_d RT_\infty D_i.$$

Now let us evaluate the last term on the right-hand side of Eq. (A2). Since $f = [\rho_\infty(2RT_\infty)^{-3/2}]\hat{f}$,

$$\int \xi_i n_i f[\ln(f/f_\infty) - 1]d\boldsymbol{\xi}$$
$$= \rho_\infty(2RT_\infty)^{1/2}\int \zeta_i n_i \hat{f}[\ln(\hat{f}/\hat{f}_\infty) - 1]d\boldsymbol{\zeta}$$
$$= \rho v_i n_i\left(\ln\frac{\rho T^{-3/2}}{\rho_\infty T_\infty^{-3/2}} + \frac{v_k^2}{2RT_\infty} + \frac{5}{2}\frac{T - T_\infty}{T_\infty}\right)$$
$$+ \frac{\rho v_j n_i}{RT_\infty}\left[-\frac{RT}{(1-\nu)A^\flat}\overline{\frac{\partial v_i}{\partial x_j}} + O(\epsilon^2)\right]$$
$$+ \frac{T - T_\infty}{T_\infty}\left[-\frac{5}{2}\frac{\rho R}{A^\flat}\frac{\partial T}{\partial X_i}n_i + O(\epsilon^2)\right]$$
$$+ \rho_\infty(2RT_\infty)^{1/2}\frac{\epsilon^2}{2}\int \zeta_i n_i\frac{(\hat{f}^{(1)})^2}{\hat{f}^{(0)}}d\boldsymbol{\zeta} + O(\epsilon^3), \tag{A8}$$

where $\hat{f}_\infty = ((2RT_\infty)^{3/2}/\rho_\infty)f_\infty$.

If we integrate Eq. (A8) over the control surface $\partial\mathcal{D}$, then each term is multiplied by $O(\mathcal{R}_d^2)$ (the order of the surface area). But using the assumption (i) again and recalling that $\epsilon = \ell_\infty/\mathcal{R}_d$, the contributions of the first three lines on the most right-hand side of Eq. (A8) are estimated as small quantities that tend to vanish as $\mathcal{R}_d \to \infty$. Since $\epsilon^3\mathcal{R}_d^2 = \ell_\infty^2\epsilon$, the contribution of the last term $O(\epsilon^3)$ on the most right-hand side of Eq. (A8) also tends to vanish in the same limit. Therefore, we are left with the term

$$\rho_\infty(2RT_\infty)^{1/2}\frac{\epsilon^2}{2}\int \zeta_i n_i\frac{(\hat{f}^{(1)})^2}{\hat{f}^{(0)}}d\boldsymbol{\zeta}.$$

But the substitution of Eq. (A7), after some manipulations, gives

$$\rho_\infty(2RT_\infty)^{1/2}\frac{\epsilon^2}{2}\int \zeta_i n_i\frac{(\hat{f}^{(1)})^2}{\hat{f}^{(0)}}d\boldsymbol{\zeta}$$
$$= -\frac{1}{4}\frac{\rho RT}{(1-\nu)(A^\flat)^2}\overline{\frac{\partial v_i}{\partial X_j}}(2A_i n_j + C_{ij}v_k n_k)$$
$$- \frac{5}{4}\frac{\rho R^2 T}{(A^\flat)^2}\frac{\partial T}{\partial X_i}(Bn_i + D_i v_k n_k) + \frac{35}{8}\frac{\rho(RT)^3}{(A^\flat)^2}D_i B n_i$$
$$+ \frac{1}{4}\frac{\rho(RT)^2}{(A^\flat)^2}(C_{ii}A_j n_j + 2C_{ij}A_i n_j)$$
$$+ \frac{7}{4}\frac{\rho(RT)^3}{(A^\flat)^2}(C_{ii}D_j n_j + 2C_{ij}D_i n_j), \tag{A9a}$$

where

$$A_i = \frac{5}{2}\frac{1}{T}\frac{\partial T}{\partial X_i}, \tag{A9b}$$

$$B = \frac{2}{3RT}\frac{\partial v_i}{\partial X_i}, \tag{A9c}$$

$$C_{ij} = -\frac{1}{RT}\left(\frac{\nu}{1-\nu}\overline{\frac{\partial v_i}{\partial X_j}} + \frac{\partial v_i}{\partial X_j} + \frac{\partial v_j}{\partial X_i}\right), \tag{A9d}$$

$$D_i = -\frac{1}{RT^2}\frac{\partial T}{\partial X_i}. \tag{A9e}$$

Because of the assumption (i), the first two lines on the right-hand side of Eq. (A9a) is $O(\mathcal{R}_d^{-2})$ multiplied by small quantities that tend to vanish as $\mathcal{R}_d \to \infty$. By the same assumption, the remaining terms are also at most $O(\mathcal{R}_d^{-2})$ multiplied by small quantities that tend to vanish as $\mathcal{R}_d \to \infty$, since they are multiplications among A_i, B, C_{ij}, and D_i. Therefore, integrating Eq. (A9a) over the control surface $\partial\mathcal{D}$ and taking the limit $\mathcal{R}_d \to \infty$ results in Eq. (A4). This concludes that Eq. (A2) is reduced to

$$\frac{d}{dt}\int_{\mathbb{R}^3}(H[f] - H[f_\infty])d\boldsymbol{X} \leqslant 0, \tag{A10}$$

and the equality holds if and only if f is a resting Maxwellian with uniform temperature T_∞.

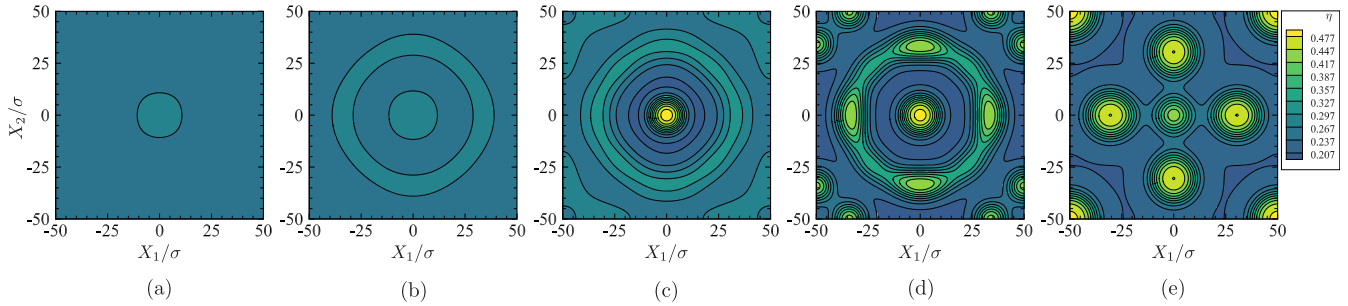

FIG. 17. Time evolution of the phase change caused by a density disturbance from the resting uniform equilibrium state with density ρ_* and temperature T_* under a spatially periodic condition in the case of $(b\rho_*, T_*/T_c) = (4/15, 0.9) = (0.266\ldots, 0.9)$ (unstable case). Contour plots of $\eta(= b\rho)$ are shown. (a) $t/t_c = 0$. (b) $t/t_c = 500$. (c) $t/t_c = 1000$. (d) $t/t_c = 2000$. (e) $t/t_c = 5000$.

APPENDIX B: GENERATION OF DROPLET OR BUBBLE INDUCED BY A PERIODIC DISTURBANCE

In Sec. IV D 1, the single droplet or bubble in the unstable region of parameters $(\eta_\infty, \tilde{T}_\infty)$ shows slow damping of the ripple of density. The feature of the slow damping might look unnatural as a physical picture. Indeed, one of the conclusions drawn in the present paper is that such a single droplet or bubble is unlikely stable and eventually collapses in a long run. However, if we pursue the time evolution from the uniform equilibrium state on the basis of the kinetic model equation after adding a disturbance at the initial time, then a similar density ripple pattern appears transiently in the unstable region. We here address such an example.

Figure 17 shows the results of a simulation that starts from an equilibrium state in the unstable region initiated by a periodic disturbance with period $2L_d$. The initial equilibrium state with the disturbance in the unit domain $|X_1|, |X_2| \leqslant L_d$ is given by

$$f = \frac{\rho}{(2\pi RT_*)^{3/2}} \exp\left(-\frac{\boldsymbol{\xi}^2}{2RT_*}\right), \tag{B1}$$

$$\rho/\rho_* = 1 + [\delta_\sigma(X_1)\delta_\sigma(X_2) - 1/(2L_d)^2]C\sigma^2, \tag{B2}$$

$$\delta_\sigma(x) = \begin{cases} \frac{1}{40\sigma}\left[1 + \cos\left(\frac{\pi x}{20\sigma}\right)\right], & (|x| \leqslant 20\sigma), \\ 0, & (|x| > 20\sigma), \end{cases} \tag{B3}$$

where $b\rho_* = 4/15(=0.266\ldots)$, $T_*/T_c = 0.9$, and $C = 1$. The present pair of parameters $(b\rho_*, T_*/T_c)$ lies deep inside the unstable region, if $(b\rho_*, T_*/T_c)$ is regarded as $(\eta_\infty, \tilde{T}_\infty)$ in Fig. 2. The computation is conducted by the same numerical code as that used in Sec. V, except that the periodic condition is applied at $|X_1|, |X_2| = L_d$ and that a correction step of the total mass, momentum and energy is inserted at every time step to retain their conservations better. In practice, the correction step had little effect on the results, but slightly improved the convergence with respect to resolution. The computational data are as follows. The quadrant of the periodic domain, $0 \leqslant X_1, X_2 \leqslant L_d$, is divided into 200×200 uniform squares with $L_d/\sigma = 50$, the truncated molecular velocity space is divided into 128×128 uniform squares, and the step size of time is $0.025t_c$. Because of the periodic condition, the system merely obeys the energy conservation and the temperature is, in general, different between the initial and the final equilibrium state at rest in the present simulation.

The radial ripple pattern of density emerges in Fig. 17(b), followed by its growth in amplitude as shown in Fig. 17(c). As the time further goes on, the pattern changes into multiple droplets with their center at the resonant points of interactions by periodicity as in Figs. 17(d) and 17(e). During this process, the temperature in the system rises from $T/T_c = 0.9$ to $T/T_c \simeq 0.95$ and the droplets creation decreases the surrounding density to $\eta \simeq 0.21 - 0.22$, causing the shift of the system from the unstable to the metastable parameter region.

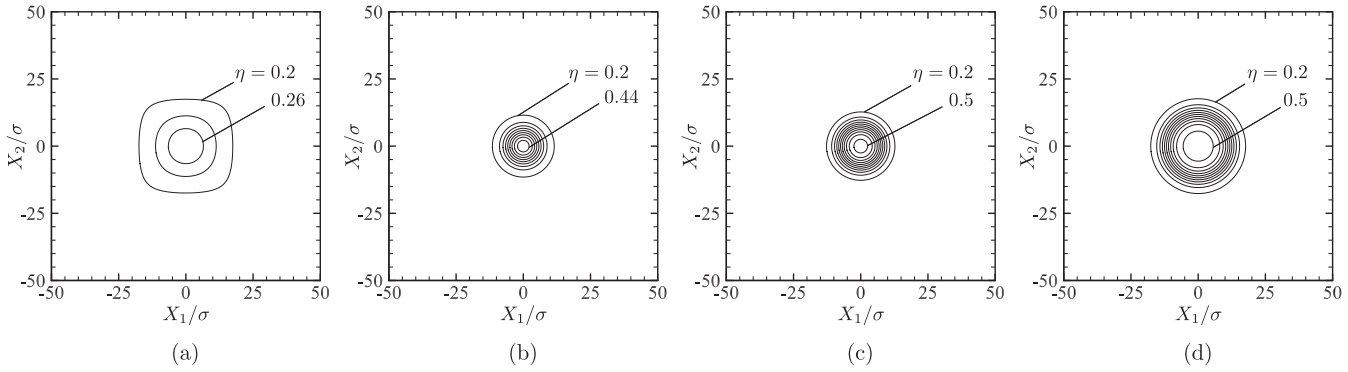

FIG. 18. Time evolution of the phase change caused by a density disturbance from the resting uniform equilibrium state with density ρ_* and temperature T_* under a spatially periodic condition in the case of $(b\rho_*, T_*/T_c) = (0.2, 0.9)$ (metastable case). Contours of $\eta(=b\rho) = 0.2 + 0.03m$ $(m = 0, 1, \ldots)$ are plotted. (a) $t/t_c = 0$. (b) $t/t_c = 500$. (c) $t/t_c = 1500$. (d) $t/t_c = 20\,000$.

The pattern in Fig. 17(e) is not yet in the final stage and the temperature is not enough uniform. After Fig. 17(e), the center droplet first collapses, and then the surrounding four droplets move to the center, unite into one droplet, and further absorb the corner droplets. The process after Fig. 17(e) was sensitive to the resolution of simulation, but in any case was finished with a single droplet in a unit periodic domain.

Figure 18 shows the results of the simulation for $b\rho_* = 0.2$, $T_*/T_c = 0.9$, and $C = 100$ for comparison. The computational domain, the discretization of space and molecular velocity, and the time step size are the same as those used in Fig. 17. A relatively large disturbance is necessary to initiate the phase change, since the new pair of parameters $(b\rho_*, T_*/T_c) = (0.2, 0.9)$ lies in the metastable region. Throughout the time evolution, the ripple of density is not observed at least at a visible level in this figure. A droplet with a radial monotone density distribution grows gradually from the initial state to the state in Fig. 18(d). During the process, the temperature in the system rises from $T/T_c = 0.9$ to $T/T_c \simeq 0.936$. In Fig. 18(d), the system has almost reached its final steady state.

[1] J. W. Cahn and J. E. Hilliard, Free energy of a nonuniform system. I. Interfacial free energy, J. Chem. Phys. **28**, 258 (1958).

[2] D. Jacqmin, Calculation of two-phase Navier–Stokes flows using phase-field modeling, J. Comput. Phys. **155**, 96 (1999).

[3] T. Inamuro, T. Ogata, S. Tajima, and N. Konishi, A lattice Boltzmann method for incompressible two-phase flows with large density differences, J. Comput. Phys. **198**, 628 (2004).

[4] M. Matsumoto, Surface tension and stability of a nanobubble in water: Molecular simulation, J. Fluid Sci. Technol. **3**, 922 (2008).

[5] M. Matsumoto and K. Tanaka, Nano bubble – size dependence of surface tension and inside pressure, Fluid Dyn. Res. **40**, 546 (2008).

[6] S. M. M. Langroudi, M. Ghassemi, A. Shahabi, and H. R. Nejad, A molecular dynamics study of effective parameters on nano-droplet surface tension, J. Mol. Liq. **161**, 85 (2011).

[7] A. Frezzotti and P. Barbante, Kinetic theory aspects of non-equilibrium liquid-vapor flows, Mech. Eng. Rev. **4**, 16-00540 (2017).

[8] S. Takata, T. Matsumoto, A. Hirahara, and M. Hattori, Kinetic theory for a simple modeling of a phase transition: Dynamics out of local equilibrium, Phys. Rev. E **98**, 052123 (2018).

[9] E. S. Benilov and M. S. Benilov, The Enskog–Vlasov equation: A kinetic model describing gas, liquid, and solid, J. Stat. Mech. (2019) 103205.

[10] V. Giovangigli, Kinetic derivation of diffuse-interface fluid models, Phys. Rev. E **102**, 012110 (2020).

[11] S. Takata, T. Matsumoto, and M. Hattori, Kinetic model for the phase transition of the van der Waals fluid, Phys. Rev. E **103**, 062110 (2021).

[12] S. Busuioc, A. Frezzotti, and L. Gibelli, A weighted particle scheme for Enskog-Vlasov equation to simulate spherical nano-droplets/bubbles, J. Comput. Phys. **475**, 111873 (2023).

[13] M. Grmela, Kinetic equation approach to phase transitions, J. Stat. Phys. **3**, 347 (1971).

[14] N. G. van Kampen, Condensation of a classical gas with long-range attraction, Phys. Rev. **135**, A362 (1964).

[15] M. Pavelka, V. Klika, and M. Grmela, *Multiscale Thermo-Dynamics: Introduction to GENERIC* (De Gruyter, Berlin/Boston, 2018).

[16] S. Takata and T. Noguchi, A simple kinetic model for the phase transition of the van der Waals fluid, J. Stat. Phys. **172**, 880 (2018).

[17] S. H. Strogatz, *Nonlinear Dynamics and Chaos* (Taylor & Francis, Boca Raton, FL, 2015).

[18] V. I. Arnold, *Ordinary Differential Equations* (MIT, Cambridge, MA, 1973).

[19] T. Miyauchi, S. Takata, M. Hattori, and A. Takahashi, Constructions of simple kinetic equations for a dense gas, in *Gas Dynamics with Applications in Industry and Life Sciences, Springer Proceedings in Mathematics & Statistics*, edited by M. Asadzadeh *et al.* (Springer, Cham, 2023), Vol. 429, pp. 19–39.

[20] A. Onuki, *Phase Transition Dynamics* (Cambridge, Cambridge, UK, 2002), Chap. 5.

[21] To discriminate from the fluid flow, the flow in the phase space is italicized in the present paper.

[22] H.-J. Butt, K. Graf, and M. Kappl, *Physics and Chemistry of Interfaces*, 3rd, revised and enlarged ed. (Wiley–VCH, Verlag, 2013).

[23] L. H. Holway Jr., New statistical models for kinetic theory: Methods of construction, Phys. Fluids **9**, 1658 (1966).

[24] P. Andries, P. Le Tallec, J.-P. Perlat, and B. Perthame, The Gaussian-BGK model of Boltzmann equation with small Prandtl number, Eur. J. Mech. B Fluids **19**, 813 (2000).

[25] D. Enskog, Kinetic theory of heat conduction, viscosity, and self-diffusion in compressed gases and liquids, in *Kinetic Theory*, edited by S. G. Brush (Pergamon Press, Oxford, UK, 1972), Vol. 3, Part 2, pp. 226–259.

[26] R. Soto, *Kinetic Theory and Transport Phenomena* (Oxford University Press, Oxford, UK, 2016).

[27] Both the spatial and molecular velocity space are originally three-dimensional. However, depending on the spatial dependence of the problem under consideration, we may set $D = 1$, 2, or 3. The droplet/bubble geometry is a sphere when $D = 3$, a cylinder when $D = 2$, and a slab when $D = 1$.

[28] It is expected by Eq. (33) that η approaches the maximum and minimum zeros monotonically. However, it approaches the middle zero oscillationally, or even oscillate eternally around it. The solution that does not approach any zeros is not appropriate as a solution of the single droplet/bubble.

[29] Equation (36) is the phase equilibrium condition in the thermodynamics such that the specific Gibbs free energy and pressure are both equal between two phases. See Ref. [11].

[30] E. Hairer, S. P. Nørsett, and G. Wanner, *Solving Ordinary Differential Equations I* (Springer, Berlin, 1993).

[31] The in-plane trajectories may cross each other as in Figs. 5(a) and 5(b) because they are projections of the original $\eta_1\eta_2\eta_3$ phase space trajectories. As a matter of course, original trajectories do not cross. The same comments applies to Figs. 6(a) and 6(b).

[32] M. Abramowitz and I. A. Stegun, *Handbook of Mathematical Functions*, 9th ed. (Dover, New York, NY, 1970), Chaps. 9 and 10.

[33] J. S. Rowlinson and B. Widom, *Molecular Theory of Capillarity* (Dover, New York, NY, 1989), Sec. 2.

[34] In the droplet case, the Gibbs radius increases with increasing η_∞ for $\eta_\infty \gtrsim 0.1725$, while it increases with decreasing η_∞ for $\eta_\infty \lesssim 0.5163$ in the bubble case; see the corresponding panel of Fig. 10. However, the results for η_∞ in these ranges are omitted in Fig. 10, since they represent the solutions with moderately varying density and the concept of interface looses its meaning.

[35] This is a parameter setting for the Sutherland model with the sixth inverse power potential and hard core of radius σ.

[36] C. K. Chu, Kinetic-theoretic description of the formation of a shock wave, Phys. Fluids **8**, 12 (1965).

[37] Y. Sone, *Molecular Gas Dynamics* (Birkhäuser, Boston, MA, 2007), Appendix A.6.

[38] J-M. Qiu and A. Christlieb, A conservative high order semi-Lagrangian WENO method for the Vlasov equation, J. Comput. Phys. **229**, 1130 (2010).

[39] L. Einkemmer and A. Ostermann, Convergence analysis of Strang splitting for Vlasov-type equations, SIAM J. Numer. Anal. **52**, 140 (2014).

[40] M. Groppi, G. Russo, and G. Stracquadanio, High order semi-Lagrangian methods for the BGK equation, Commun. Math. Sci. **14**, 389 (2016).

[41] S. Takata, Y. Sone, and K. Aoki, Numerical analysis of a uniform flow of a rarefied gas past a sphere on the basis of the Boltzmann equation for hard-sphere molecules, Phys. Fluids A **5**, 716 (1993).